

DTIC FILE COPY

4

AD-A201 347

FINAL TECHNICAL REPORT

INTENSIFIED BISTABLE OPTICAL DEVICE

CONTRACT NO.: N00014-87-C-0747

SUBMITTED TO: Dr. William Miceli
Mathematical Sciences Division
Office of Naval Research
800 N. Quincy Street
Arlington, VA 22217-5000

SUBMITTED BY: Optron Systems, Inc.
3 Preston Court
Bedford, MA 01730

DATE: 8 August 1988

DTIC
S ELECTE D
OCT 19 1988
H

UNCLASSIFIED

DISTRIBUTION STATEMENT A

Approved for public release;
Distribution Unlimited

Certification of Technical Data Conformity

The Contractor, Optron Systems, Inc., hereby certifies that, to the best of its knowledge and belief, the technical data delivered herewith under Contract No. N00014-87-C-0747 is complete, accurate, and complies with all requirements of the contract.

Date

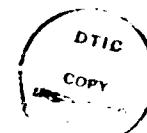
August 88

Name and Title of Certifying Official

Jeffrey K. Bound, P.E. and Sr. Research Scientist

TABLE OF CONTENTS

Certification of Technical Data Conformity	ii
Table of Contents	iii
I. Background	1
II. Overall Project Goals	2
A. The Ideal Bistable Optical Device	2
B. IBOD Description and Principles of Operation	4
III. Phase I Objectives	6
IV. Summary of Work Accomplished	7
V. Technical Results	11
A. IBOD Theory: The Monopixel IBOD Model	12
B. Device Characteristic Measurement Apparatus	19
C. Device Characteristic Measurement Procedure	24
D. Experimental Results	27
E. Analysis of Results	27
1. Resolution	27
2. Temporal Dependence	39
3. Control Bias Dependencies	40
VI. Recommendations for Future Work	44
VII. Phase I Conclusions	49
VIII. References	51
IX. Appendix	52



By <i>per letter</i>	
Distribution/	
Availability Codes	
Dist	Avail and/or Special
A-1	

I. BACKGROUND

Optical computers are potentially critical elements in meeting the intense battle management computation requirements of the SDI program. The current lack of high-speed, high-resolution nonlinear light modulation devices limits the performance of and utility of all-optical computation machines. Such devices are needed to implement a variety of important functions, including associative memory, optical neural networks, optical logic, pattern recognition, programmable spatial filtering, intensity thresholding, intensity level slicing, and edge enhancement. Device development must therefore play a critical role in establishing the feasibility of high-performance optical computer systems.

The development of a two-dimensional array of fast, optically triggered light switches that requires low optical switching power, exhibits high switching speed and high resolution and that is cascadable with itself and other optical computer components would significantly enhance the current state-of-the-art in optical computing. The work described herein concerns the development of such a nonlinear spatial light modulator. This device is inexpensive, offers high resolution, high speed, low optical switching power, operates at room temperature, and is rugged, reliable, and easily manufactured.

Optical bistable devices will be useful in optical computers because they can potentially be used as fast optical switches. Optical bistability has been demonstrated in a large number of materials in recent years, but most of the devices built so far either operate at low temperature, exhibit too large a switching energy to be useful for two-dimensional spatial light modulators, or consist only of a few resolution elements. Room temperature bistability has been achieved in semiconductor materials such as GaAs-GaAlAs, GaAs, InSb, InSe and InGaAsP/InP.¹⁻⁶ Switching times range from as low as 10 picoseconds for GaAs multiple quantum well devices to a few milliseconds in InSe. Thus far, only small arrays (approximately 10×10) of devices have been built, and it appears that this technology does not easily permit scaling to millions of devices in a two-dimensional array on a single chip. Furthermore, the optical power required to switch these devices at nanosecond rates varies in the range between 10 mW/cm^2 for InGaAsP/InP and 100 kW/cm^2 for InSb. Thus unacceptable optical power levels would be required to operate a spatial light modulator containing millions of these devices at nanosecond speeds.

Optron Systems' Intensified Bistable Optical Device (IBOD) represents a novel approach to nonlinear optical device design. The IBOD is essentially a second generation image intensifier tube that employs channelized optical feedback between the luminescent phosphor layer and the photocathode. This approach does not suffer from the resolution and scaling problems that plague the above-mentioned semiconductor technologies, and it leads to devices that are simple and inexpensive to manufacture. Consequently, this device could potentially be mass-manufactured at very low cost.

The ultimate objective of the IBOD development program is a device which would exhibit the following features:

- Fast switching speeds ($\sim 10^3 \text{ Hz}$),
- Bistable spatial light modulation and long-term latching,
- High gamma (~ 10),

- Room temperature operation,
- High resolution ($\sim 10^6$ pixels in a 25mm diameter active area),
- Low optical switching energy ($\sim 10^{-15}$ J/element),
- Large optical gain ($\sim 10^4$),
- Triggering with either coherent or incoherent input light,
- Excellent artifact noise immunity in output signal (output light is incoherent),
- Complete cascability with itself and other spatial light modulators,
- Low electrical power consumption ($\sim 10^{-7}$ W/pixel),
- Electrical erasure (no optical flood beam necessary),
- Self-luminous readout,
- Fiber-optic faceplate technology to permit easy coupling to other optical components in a system,
- Proven ruggedness and reliability inherited from its similarity to current mil-spec image intensifiers, and,
- Low cost of manufacture ($\sim \$5000$ each in quantities of 100 or more).

This final report covers Phase I work intended to demonstrate feasibility of concept and provide direction for additional phases in the device development program.

II. OVERALL PROJECT GOALS

A. The Ideal Bistable Optical Device

The ultimate goal of the Intensified Bistable Optical Device (IBOD) Program is to produce a high-gain, optical-input, optical-output, high-speed, high-resolution device exhibiting a bistable input-output curve, with over one million pixels behaving independently. For the purposes of this report we define bistability as shown in Figure 1. Figure 1a shows an example of the input-output curve of a monostable system. Note that the output is determined uniquely by the input; that is, for a given input, the output value is uniquely known with no additional information. In contrast, Figure 1b shows an example of the input-output curve of a bistable system. The device exhibits memory, so that the output is not uniquely determined by the input, but also depends on the history or state of the device.

A familiar example of a bipolar bistable device is the Schmitt trigger op-amp circuit shown in Figure 2a. The device input-output curve (shown in Figure 2b)

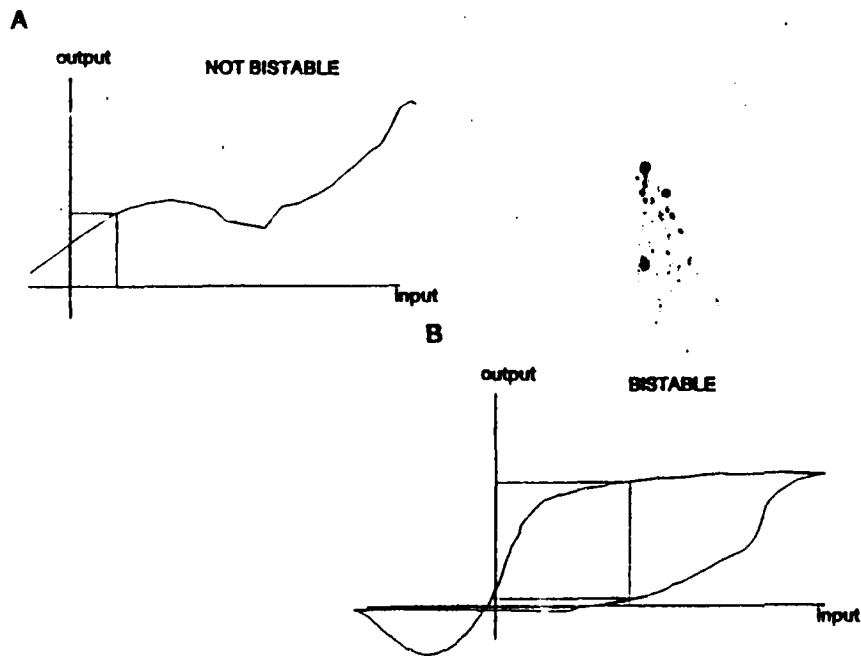


Figure 1. Definition of Bistability: A) monostable input-output curve; B) Bistable input-output curve.

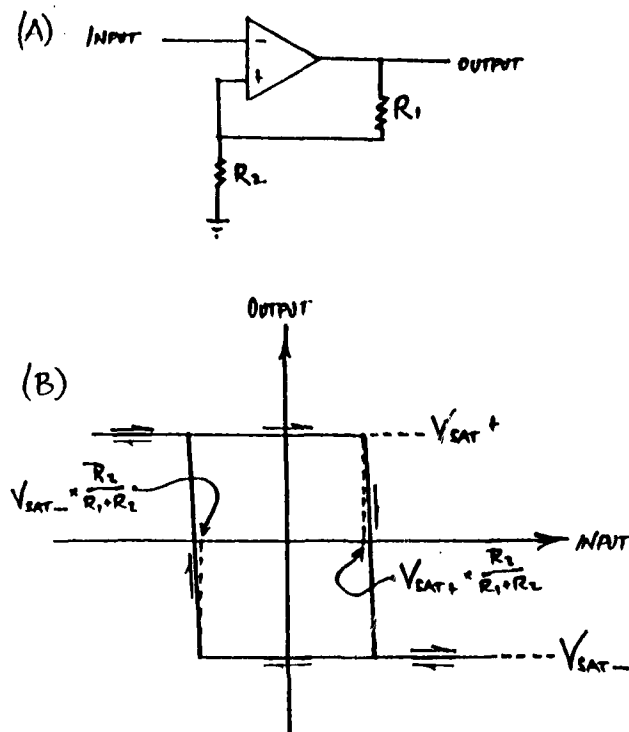


Figure 2. The Schmitt Trigger. A) Circuit; B) Input-Output Curve.

exhibits a particular form of bistability known as hysteresis: the input must be overdriven to force the output from one state into the other.

The ideal bistable optical device input-output curve differs subtly from that of the Schmitt trigger. Since the optical device is driven by optical intensity, rather than by bipolar field strength, there are no negative values for either input or output. Figure 3 shows the ideal characteristic for a single pixel of the proposed Intensified Bistable Optical Device. The output starts in the OFF state with an output intensity near zero. When the input reaches some threshold intensity I_T , the output switches to the ON state, with a high output intensity level. Beyond this input value, the output remains saturated at some value I_{SAT} . If the input is then reduced below the threshold intensity I_T , the output remains saturated at I_{SAT} . The output is returned to its off state by an external reset; that is, once turned on, the pixel cannot be turned off by the optical input. An ideal device would comprise many such pixels, each operating on its input independently of all other pixels.

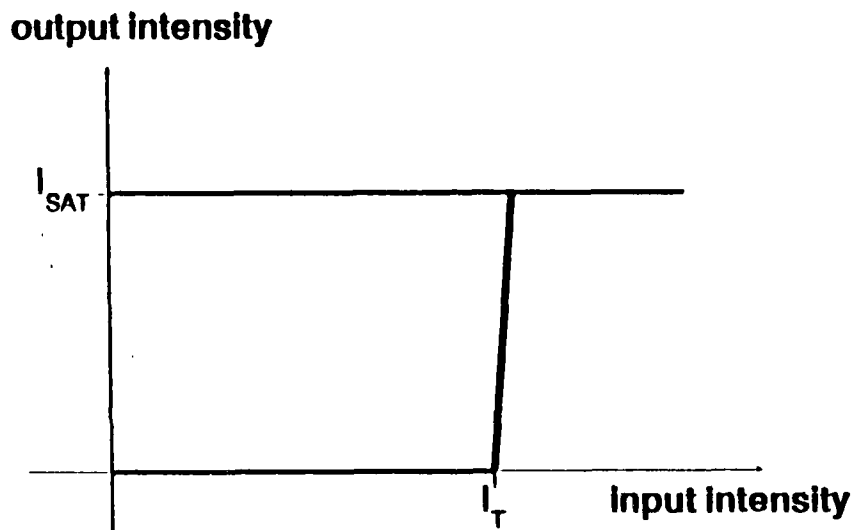


Figure 3. Ideal Input-Output Curve of a Bistable Optical Device.

B. IBOD Description and Principles of Operation

The Intensified BOD being developed by this program is expected to comprise about 3×10^5 pixels in an active area of roughly 2.5 cm^2 . The IBOD architecture, illustrated in Figure 4, is based on the second-generation image intensifier tube technology employed in modern night vision goggles. From this technology the IBOD inherits high resolution, high optical gain, compact dimensions, and a large-scale manufacturability. By sharing as many components and construction techniques as possible with the second-generation tubes, IBOD fabrication costs can be kept low without sacrificing performance.

As shown in Figure 4, the IBOD consists of three active components. A photocathode is constructed over the input fiber-optic faceplate; a microchannel

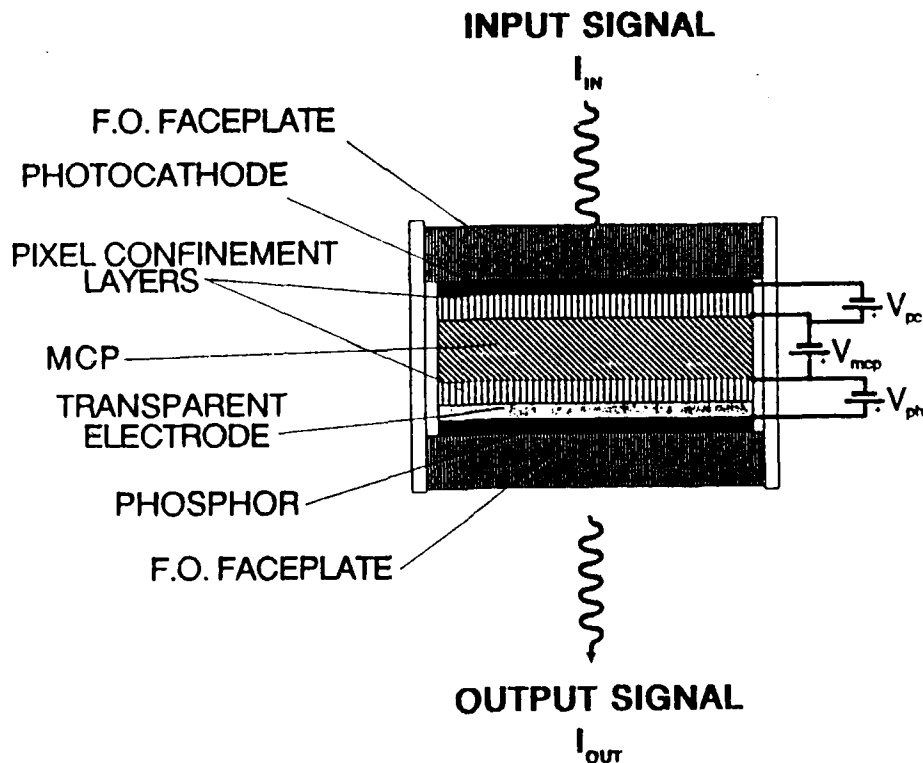


Figure 4. Architecture of the IBOD.

electron multiplier plate (MCP) is mounted approximately in the center of the device; and a phosphor screen and transparent electrode are constructed over the output fiber-optic faceplate. Pixel confinement layers fill the space between the photocathode and MCP and between the MCP and phosphor screen. The components are mounted in a cylindrical case which is evacuated and vacuum-sealed. Electrode contacts for the photocathode, MCP, and phosphor screen penetrate the case for connection with external bias voltages. The device is normally biased externally with power supplies as shown in the figure.

Basic signal paths through the device are shown in the flow diagram of Figure 5. Consider a single pixel of the device. Input light strikes the photocathode, and the photons are converted to electrons with efficiency $\eta(\lambda)$. The resulting photoelectrons are driven to the input face of microchannel electron multiplier plate (MCP) by an electric field maintained between the photocathode and MCP input face by the external supply. As the photoelectrons propagate through a channel of the MCP, they are multiplied by secondary emission on impact with the sides of the MCP channel. At the output of the MCP, the amplified signal emerges as a large number of electrons. These electrons are accelerated toward the phosphor screen by a strong potential difference between the MCP and the screen. For a sufficiently large number of electrons, the kinetic energy of the electrons is converted to light on impact with the screen with some efficiency ρ . Some of the resulting photons leave the device through the fiber-optic output plate, but others propagate back to the MCP. Those photons axially aligned with MCP channels successfully propagate backward through the MCP and strike the photocathode. At the photocathode these feedback photons are converted to electrons with wavelength-dependent quantum

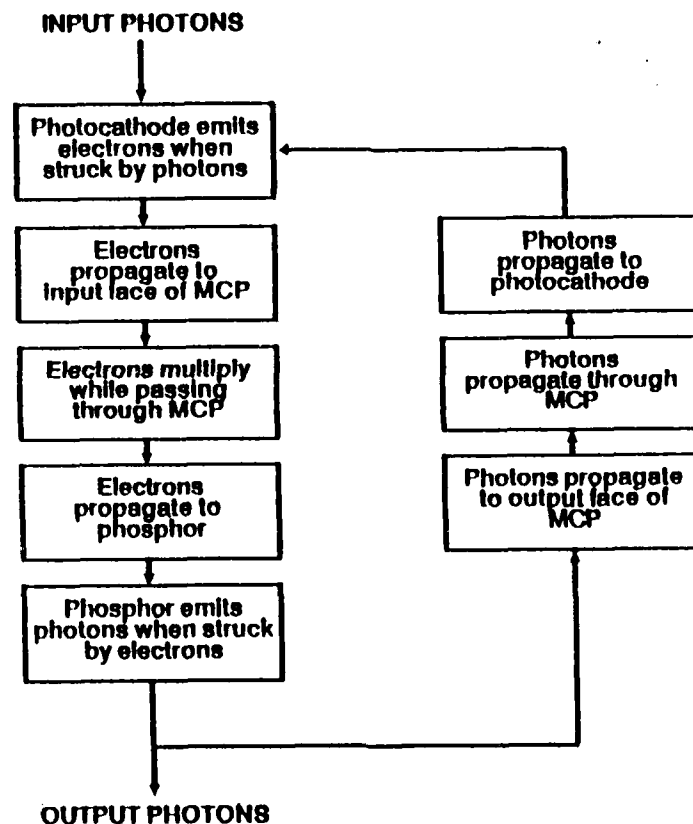


Figure 5. Signal Flow through the IBOD.

efficiency $\eta(\lambda)$. The resulting photoelectrons are again driven into the MCP, and the cycle continues. If the roundtrip gain experienced by the signal is greater than unity, the signal will grow until some component of the device saturates. The feedback signal will then be sufficient to keep the phosphor screen lit even when the input signal is removed. This state, with the phosphor lit regardless of input, is referred to as the ON state. The complementary state, with insufficient input to light the output, is called the OFF state. The behavior of the device is discussed in greater detail in the Technical Results section.

III. PHASE I OBJECTIVES

The underlying goal for this six-month Phase I IBOD program was to prove the viability of the IBOD concept and collect sufficient information to make a fruitful Phase II development effort possible. Five Phase I objectives were devised to meet this goal:

- Design and construct a series of prototypes to demonstrate the bistable behavior of the IBOD architecture.
- Model device behavior to the extent necessary to provide an understanding of parameters influencing device performance.

- Once bistability has been achieved, study resolution of prototypes to determine severity of anticipated crosstalk-induced pixel blooming problem.
- Design and construct an additional prototype incorporating pixel confinement structures as necessary to demonstrate multi-pixel resolution.
- Make detailed measurements of performance and operational dependencies of final prototype.

The initial intent was to produce a series of prototypes, with each succeeding design adding or perfecting a new feature, culminating in the design and construction of a prototype providing multipixel bistable performance.

IV. SUMMARY OF WORK ACCOMPLISHED

An agreement was made with Varo, Inc., a Garland, Texas-based manufacturer of second-generation image intensifier tubes, to construct prototypes based on design modifications to their proven second-generation image tube architecture. Varo's ability to construct tubes allowed us to avoid costly duplication of existing technology by making use of Varo's appreciable know-how and tube fabrication expertise.

The agreement with Varo proved to be good for the Phase I work, as the prototypes produced by Varo were of near-production quality and quite well packaged. Of a total of six prototypes devices, none experienced problems due to construction flaws. In addition, a great deal of time was saved, as Varo was able to deliver the first prototype within a month of the final design completion.

As the first prototypes were intended only to demonstrate bistability, the design of the first prototype, illustrated in Figure 6a, employed no pixel confinement layers. Instead component spacing was kept as small as possible with production line components. This was done so that the first prototype could be constructed as quickly as possible; addition of pixel confinement structures would have made production-line construction impossible and significantly delayed completion. In addition, it was decided that the anticipated pixel-blooming problem should be studied in its native form without the complication of additional structures to confuse the issue. In this way a determination of the seriousness and extent of the problem could be made before a solution was attempted. In this vein, during construction of the prototype, studies were made of the characteristics of light transmission through the MCP to determine the severity of optical crosstalk that should be anticipated. Results of this study showed that the MCP would reduce optical crosstalk to some extent, but, even at the smallest component spacings attainable on Varo's production line, probably not sufficiently to eliminate the crosstalk problem.

Unfortunately, when the first prototype arrived, it was found that the device had actually been built as shown in Figure 6b; due to a miscommunication the phosphor

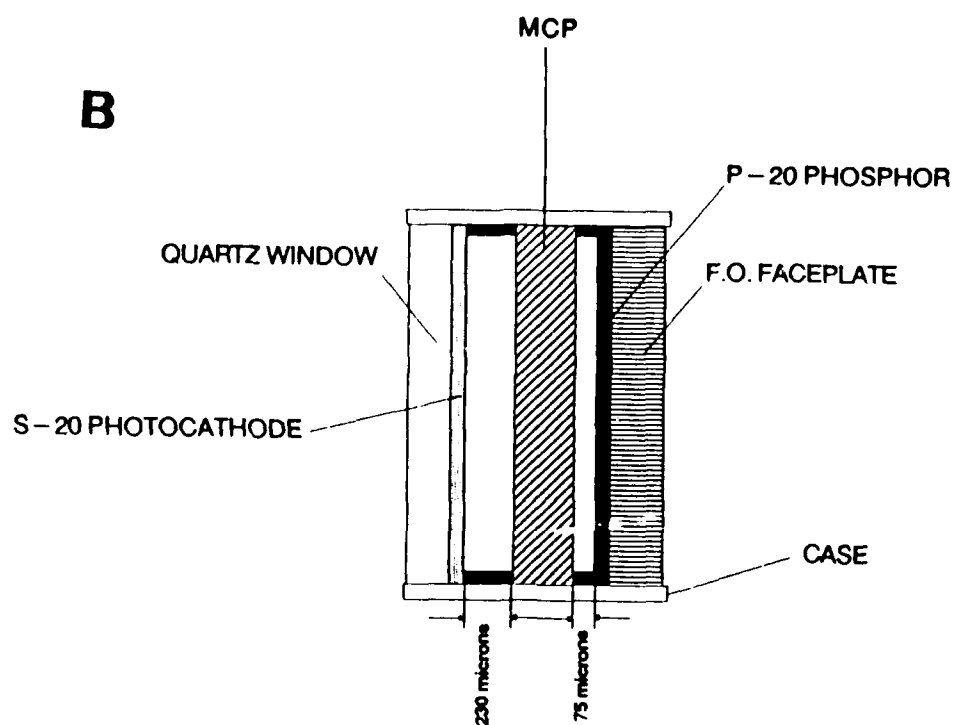
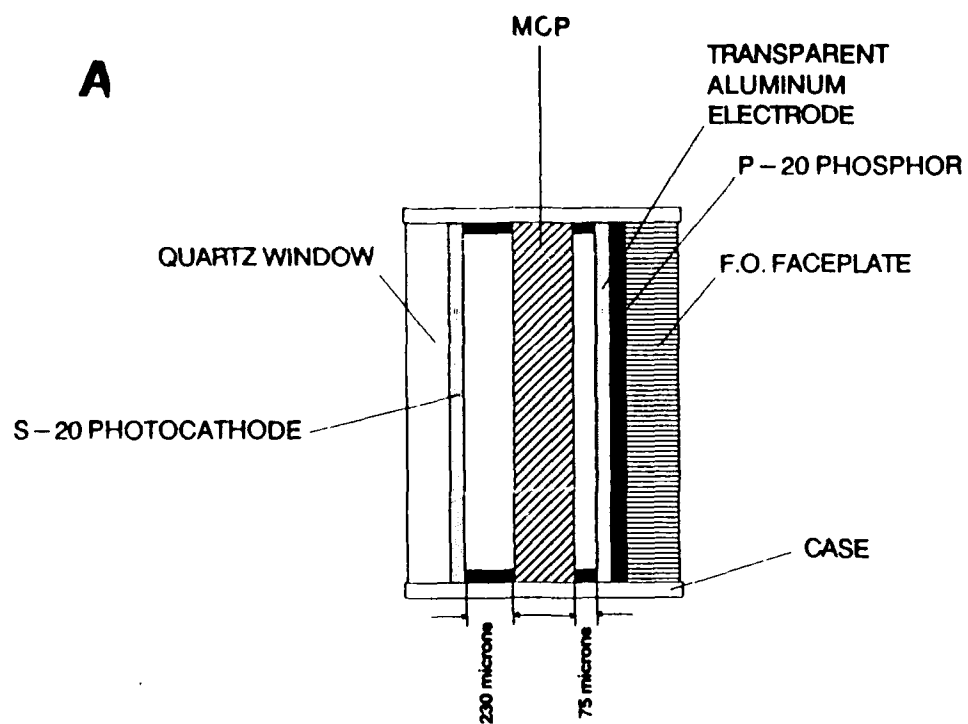


Figure 6. The First IBOD Prototype. A) As designed; B) As constructed.

electrode was completely omitted. Nevertheless, a crescent-shaped portion of the output of the device eventually functioned sufficiently to demonstrate bistability.

A second prototype was fabricated according to the design of Figure 6a; the requested phosphor aluminum electrode thickness was 300Å. Two samples of this prototype were constructed. Neither device proved bistable, even after prolonged testing in search of a bistable operating point. Later inspection with a laser indicated that the aluminum electrode layer on the phosphor was virtually opaque—too thick to transmit sufficient feedback light to allow bistable operation. It became clear that some alternative had to be found to the aluminum layer, as an aluminum layer sufficiently thin to allow optical feedback would be too resistive to function adequately as a phosphor electrode.

The problem of phosphor electrode opacity was addressed with the third and fourth prototype designs, which were constructed and evaluated simultaneously. Both devices reverted to the standard second-generation tube component spacings to minimize turnaround time and avoid added complications. The third prototype, shown in Figure 7a, employed a transparent layer of Indium-Tin-Oxide (ITO) over the phosphor to serve as phosphor electrode. The fourth prototype, shown in Figure 7b, employed a transparent layer of ITO over the fiber-optic output with the phosphor layer constructed over the ITO. Both devices were designed to introduce the least possible attenuation into the optical feedback path while providing the necessary conductivity for proper operation of the phosphor screen.

Both devices exhibited bistable behavior over large areas of their outputs, but only after the devices had accumulated several minutes of ON time in the course of testing. The ITO-over-phosphor device of Figure 7a arced internally, raising doubts about its longevity. The ITO-under-phosphor device of Figure 7b showed no signs of arcing.

With both these devices, all the bistable areas of the output of the device turned on together, even when only a small area of the input was exposed to an input signal. This was assumed to be a manifestation of the anticipated crosstalk-induced pixel blooming. For input signals very near threshold intensity, it was found that the pixel blooming process occurred at observable speeds. Based on these observations, a fifth prototype was fabricated as in Figure 8—identical to the ITO-under-phosphor device of Figure 7b, but with the smallest separation between MCP and phosphor screen that Varo could produce quickly. Also, while the earlier prototypes had been constructed with slightly noisy MCPs to reduce turnaround time, the fifth prototype was to be constructed with a low-noise MCP. Our intention with the fifth prototype's design was to determine the effect on pixel-blooming of the reduced component spacing. As fabrication time for this fifth prototype was quite long, it was decided to make this the final prototype for the Phase I program and to test it extensively to learn as much as possible from the device.

Curiously, the fifth prototype did not initially exhibit bistable behavior; only after the device had experienced several minutes of accumulated ON time did portions of the device output achieve bistability. It was at this point in the program that the importance of device aging became evident. Not one of the devices had exhibited bistability until it had accumulated several minutes of ON time, but initially this effect had been attributed to difficulty in finding the correct combination of control bias voltages to attain a bistable operating point. The experience with the fifth prototype led us to strongly suspect an aging phenomenon; careful inspection of the fourth prototype confirmed the suspicion. This fourth prototype had been

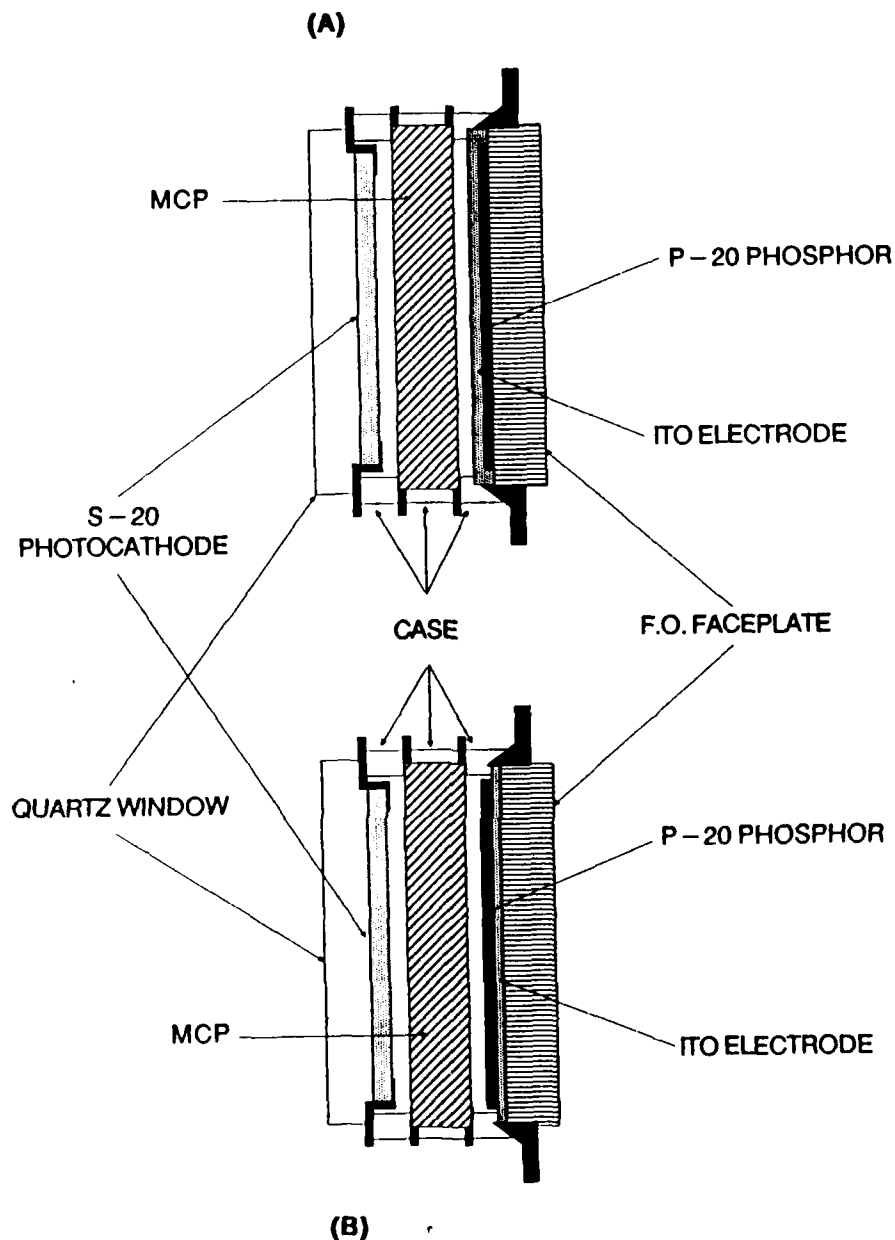


Figure 7. IBOD prototype designs. A) Third IBOD prototype design; B) Fourth prototype design.

tested with a mask covering portions of the input; only the areas of the output of the device corresponding to the input areas exposed by the mask became bistable. Even after the mask was removed, only those areas which had been exposed by the mask initially showed bistability. The other areas slowly began to exhibit bistability only after the device had been tested extensively without the mask.

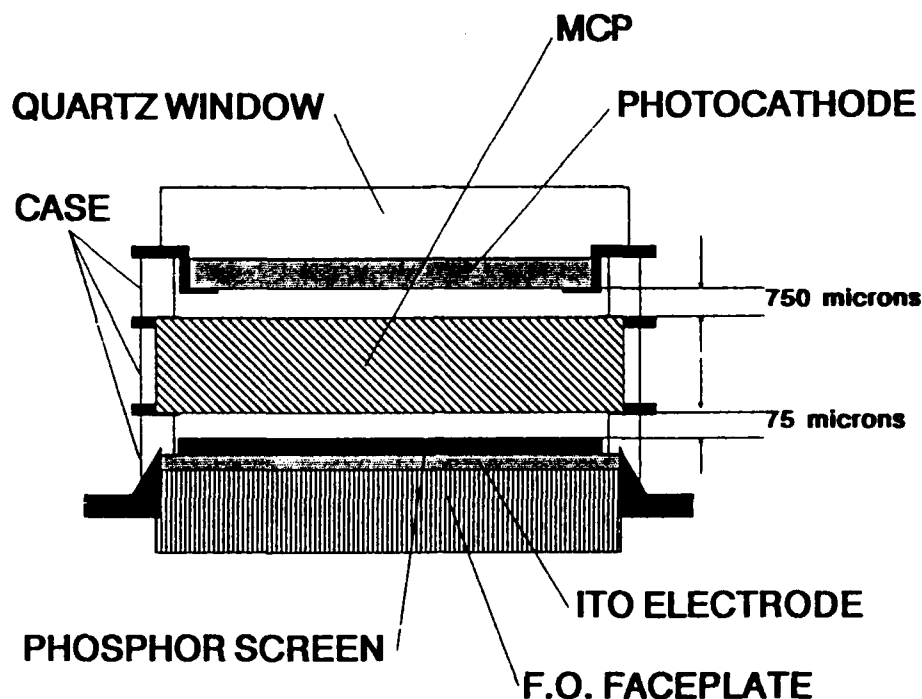


Figure 8. Design of the Fifth and Final Prototype.

Once the fifth prototype had exhibited bistability, the behavior of the device was carefully studied. As expected, the pixel bloom rate appeared somewhat slower in the fifth prototype than in the fourth, taking on the order of a second to cover the entire active area for inputs very near threshold. A test jig was constructed for the measurement of the input-output characteristic of the fifth prototype. The relationship between the input-output characteristic and the three control biases was carefully explored with several series of traces. The results were compared with the behavior predicted by the monapixel IBOD model, which had been developed during the construction of the prototypes. The model was modified and additional measurements of the prototype made until it was felt that we had a good understanding of the relationship between control voltages and the behavior of the IBOD. Finally, traces were made of the input-output characteristic of the fourth prototype for comparison with the measured behavior of the fifth prototype. Observations and measurements made on the fourth and fifth prototypes are discussed in detail in the Technical Results section.

V. TECHNICAL RESULTS

This section is a technical report of all the major results of the IBOD Phase I program. It includes a complete discussion of both the monapixel IBOD model and of the results of experimental measurement of the input-output characteristics of the fourth and fifth prototypes. We begin with a discussion of the theory behind the operation of the IBOD, developing a model to predict the device's behavior in subsection A. In subsections B and C we describe the experimental apparatus and the experimental procedure used to measure prototype characteristics. Subsection D

presents the experimental results, including both raw data and pertinent plots. We conclude in subsection E with an analysis of the data obtained.

A. IBOD Theory: The Monopixel IBOD Model

In this section we elaborate upon the description of the basic operation of the IBOD of Section II. We develop a simple model for the behavior of a single independent pixel of the IBOD and predict the device's behavior based on the model.

Consider the signal flow diagram of Figure 9. Let us derive a mathematical representation of the IBOD signal paths in the absence of nonlinearity. That is, we treat the IBOD as though all of its components were ideally linear, ignoring turn-on and saturation nonlinearities. The photocathode converts impinging photons to electrons with wavelength-dependent quantum efficiency $\eta(\lambda)$. The resulting photoelectrons propagate to the input face of the MCP and enter the channels of the MCP with a propagation loss γ . This figure reflects largely the loss of electrons to the solid area of the MCP input electrode. The electrons are multiplied in the MCP by a gain factor G . Electrons emerging from the MCP are accelerated toward the phosphor with potential V_{ph} and are converted back to photons at efficiency $\rho(V_{ph}, \lambda)$; the phosphor conversion efficiency varies across the spectrum and with accelerating potential V_{ph} . Some fraction of the generated output light successfully propagates back through the MCP to the photocathode, where the photons are converted back to electrons with efficiency $\eta(\lambda)$. The propagation loss associated with this feedback path is β . Finally, both the photocathode and the MCP produce dark currents which we represent with current i_d injected into the signal stream after the photocathode. Current i_d is therefore the sum of the photocathode dark current and the MCP dark current referenced back to the photocathode.

Note that, since the quantum efficiency of the photocathode is wavelength dependent and the input and feedback signals will, in general, have different spectrums, in the most general case the input and feedback signals should be multiplied by different effective quantum efficiencies η_{in} and η_{fb} , respectively, given by

$$\eta_{in} = \frac{\int \eta(\lambda) \cdot \lambda \cdot S_{in}(\lambda) d\lambda}{\int \lambda \cdot S_{in}(\lambda) d\lambda} \text{ and } \eta_{fb} = \frac{\int \eta(\lambda) \cdot \lambda \cdot S_{fb}(\lambda) d\lambda}{\int \lambda \cdot S_{fb}(\lambda) d\lambda}, \quad (\text{EQ 1a\&b})$$

where λ is wavelength, $\eta(\lambda)$ is the wavelength-dependent quantum efficiency of the photocathode, $S_{in}(\lambda)$ is the power spectrum of the input signal, and $S_{fb}(\lambda)$ is the power spectrum of the optical feedback signal (i.e. of the phosphor). For simplicity, however, we ignore the differences in sensitivity of the photocathode to input and feedback signals and use a single value, η .

Table I shows typical, computed, and assumed values for the linear device parameters and the sources of the values. The figures for η and ρ were obtained by choosing an average value over the wavelengths of interest. The figure for β was obtained from measurements made of optical transmission through the MCP (see Appendix). The figure for γ is based upon the open area of the MCP and assumes no other source of loss.

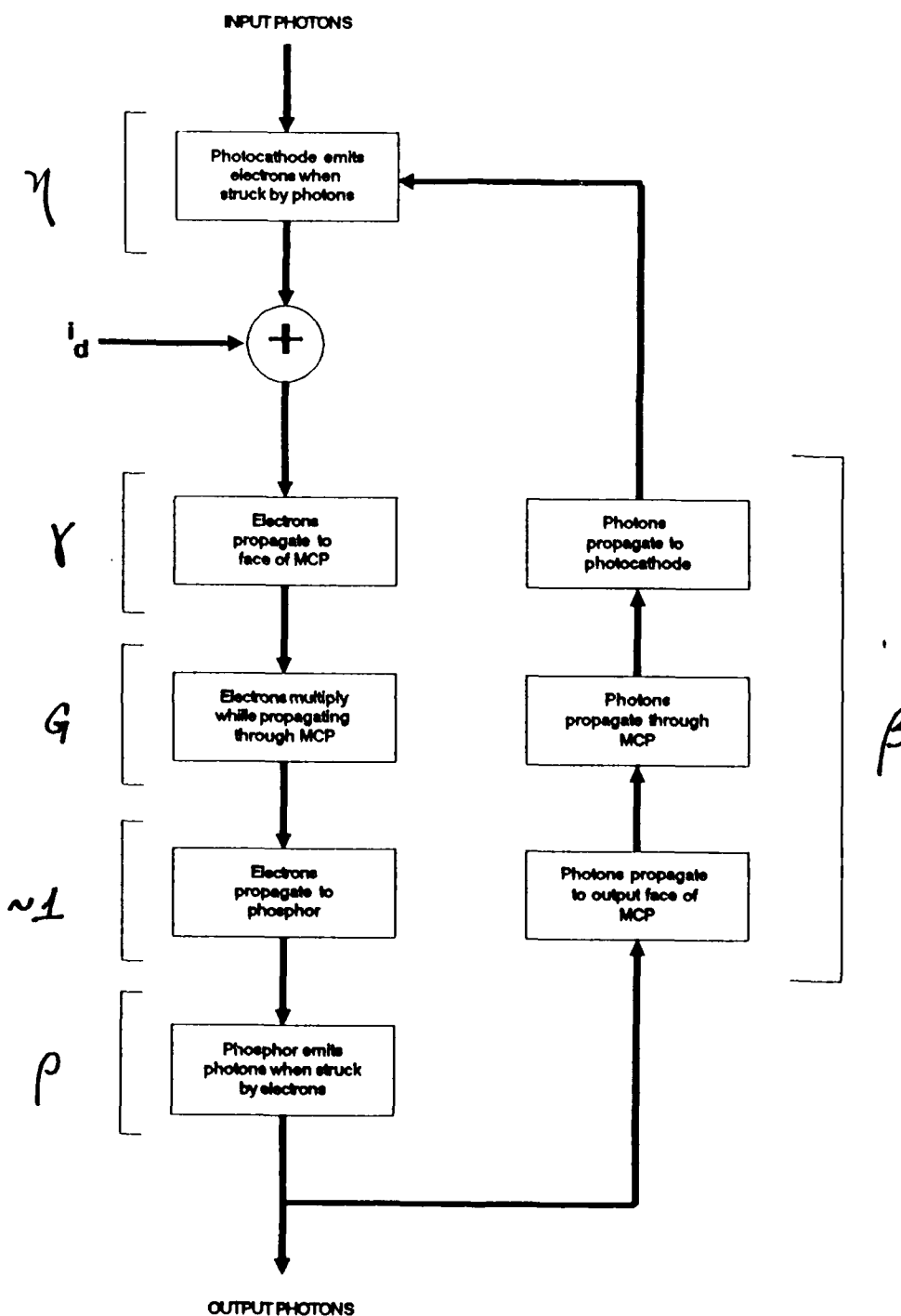


Figure 9. Signal Path through the IBOD and Associated Gain or Loss Factors.

SYMBOL	PARAMETER	VALUE	NOTES
η	Photocathode quantum efficiency	10%	Ballpark
ρ	Phosphor conversion efficiency	4.5×10^{-2} photons/electron	Ballpark
G	MCP current gain	10^3	Function of MCP voltage
γ	Electron propagation loss, PC-to-MCP	50%	Based on Open Area of MCP
β	Photon loss, phosphor-to-PC	0.163%	Ignores crosstalk and edge losses
I_d	Total dark current, referenced to photocathode	4×10^{-15} A	Typical figure

Table 1. Linear Device Parameters of the Monopixel IBOD Model.

We arrive at the monopixel model of the IBOD by combining the above linear signal flow model with two nonlinear elements, one representing thresholding and the other saturation. There are two reasons for separating out the nonlinearities from the linear components of the model. First, the actual sources of the nonlinearities are not known with certainty. Saturation is possible in either the photocathode, the MCP, or the phosphor screen; which component (or combination of components) is responsible for the observed device saturation is not known, though the photocathode seems an unlikely source. In addition, little documentation of the thresholding nonlinearity exists, and, though the phosphor is suspected as the source, little evidence exists to rule out the other two components. The second reason for isolating the nonlinearities into separate components is simplicity. We model both threshold and saturation nonlinearities as simply as possible.

The transfer function $T(x)$ of the ideal thresholding component required in the IBOD monopixel model is shown in Figure 10. The thresholding component allows the IBOD to ignore inputs below a certain value and is responsible for the turn-on

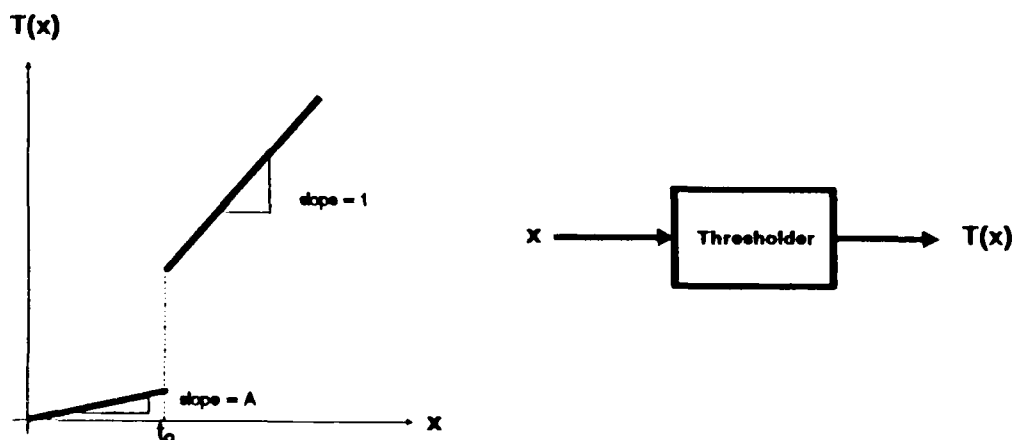


Figure 10. An Ideal Thresholding Element.

characteristic of the device. For simplicity we define the function by

$$T(x) = \begin{cases} Ax & \text{for } x \leq t_o, \\ x & \text{for } x > t_o \end{cases} \quad (\text{EQ 2})$$

where $0 \leq A < 1$. Thus we represent the threshold nonlinearity as an increase in gain from A , when the input is below threshold t_o , to 1, when the input is above t_o .

The saturation component limits the value of the output of the IBOD in the ON state. The function is defined by

$$S(x) = \begin{cases} x & \text{for } x \leq s_o, \\ D \cdot (x - s_o) + s_o & \text{for } x > s_o \end{cases} \quad (\text{EQ 3})$$

where $0 \leq D < 1$. The saturation transfer function is illustrated in Figure 11.

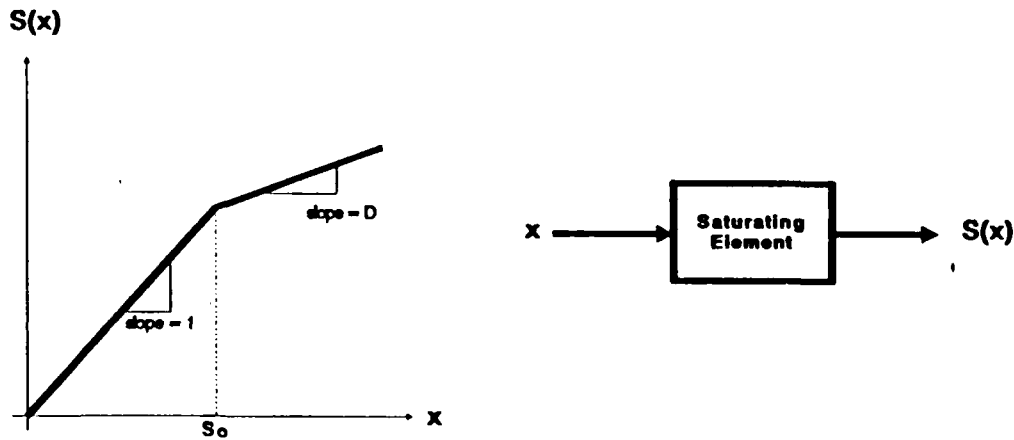


Figure 11. An Ideal Saturating Element.

We can construct a simple monapixel model for the IBOD's behavior by combining the linear signal path parameters into four linear gain and loss elements and adding the two nonlinear components as shown in Figure 12. The various signals are labelled and identified in the figure. The four linear elements are the forward gain H , the feedback loss J , the optical-to-electrical loss η , and the output loss P . The optical-to-electrical loss η represents the quantum efficiency of the photocathode; the forward gain H represents the loss of electrons from photocathode to MCP, the gain in the MCP, and the phosphor conversion efficiency; and the feedback loss J represents the losses associated with propagation from the phosphor through the MCP to the photocathode. The output loss P represents the geometric losses associated with coupling into the fiber-optic faceplate. We can write H and J in terms of linear device parameters previously defined:

$$H = \rho \gamma G V_{ph}; \quad (\text{EQ 4})$$

$$J = \beta. \quad (\text{EQ 5})$$

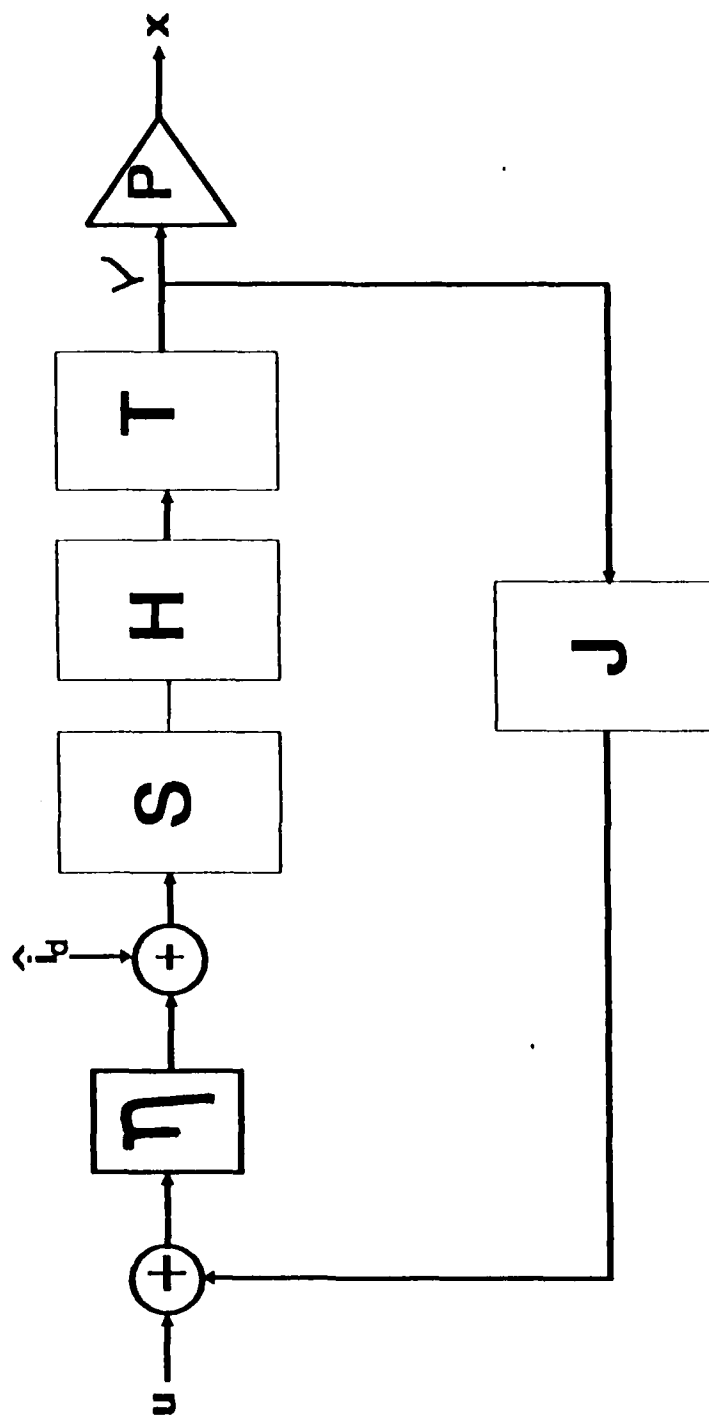


Figure 12. Block Diagram of the Monopixel IBOD Model.

Note that the nonlinear components are placed somewhat arbitrarily in the model since their real sources are unknown. While the placement of these components makes some quantitative difference in the predicted behavior of the model, the general form of the behavior is essentially independent of placement of these components in the signal paths.

Now let us consider the behavior predicted by the monapixel IBOD model. We take advantage of the piecewise linearity of the nonlinear elements and divide the operating range of the device into individually linear regions. To do this we assume that the thresholding component reaches its threshold before the saturating component reaches its saturation level; that is, we assume that $Hs_o > t_o$. Thus we can divide the operating range into three regions: the off region, wherein the thresholding component is in its low-gain operating range; the switching region, wherein both the thresholding and the saturation components are in their high-gain operating ranges; and the on region, wherein the saturation component is in its low-gain operating range. We consider each of these regions separately.

Assume that the IBOD is operating in the off region, so that $t < t_o$ and $s < s_o$. Let us solve for v where v is defined as in Figure 12 to be the photon flux generated by the phosphor. We obtain the equation

$$v = T(t) \Big|_{t = H \cdot S(s) < t_o; s < s_o} \quad (\text{EQ 6})$$

$$= A \cdot H \cdot S(s) \Big|_{s = \hat{i}_d + \eta \cdot (u + Jv) < s_o} \quad (\text{EQ 7})$$

$$= \eta HJA v + HA \cdot (\hat{i}_d + \eta u), \quad (\text{off region}) \quad (\text{EQ 8})$$

where u is the input flux of photons into the IBOD and \hat{i}_d is the electron flux produced by the dark current referenced to the photocathode. Recall that \hat{i}_d , u , and v must be non-negative since they represent essentially numbers of events. We must therefore require that $\eta HJA \leq 1$ for a solution to exist. We can see from the signal path diagram why this must be so. Note that the quantity ηHJA is the total loop gain in the off region; that is, ηHJA is the gain experienced on one round trip by a signal traversing the feedback loop of the IBOD when the IBOD operates in the off region. For values of loop gain greater than one, the output v grows as the signal traverses the feedback loop repeatedly, until at some point the input to the thresholding component exceeds t_o and the device leaves the off region.

We can solve the above equation for v for values of off-region loop gain less than one. Solving and using $x = Pv$, we find the output to be given by

$$x = \frac{PAH \cdot (\hat{i}_d + \eta u)}{(1 - \eta AHJ)} \quad (\text{off region}) \quad (\text{EQ 9})$$

In the off region, then, the output of the device consists of a term proportional to the input and an additive noise term generated by the dark current of the device. Under the assumption of an off-region loop gain of less than one, this linear relationship between input and output holds until the input to the thresholding component reaches the switching value of t_o . Straightforward computation shows that

the corresponding input required to attain this value at the thresholding component's input is given by

$$u_o = \frac{t_o \cdot (1 - \eta AHJ) - \hat{i}_d}{\eta H} \quad (\text{switching threshold}) \quad (\text{EQ 10})$$

At input values above this the device enters the switching region, so that $t > t_o$ and $s < s_o$. Solving for v in this region we find

$$v = T(t) \Big|_{t = H \cdot S(s) > t_o; s < s_o} \quad (\text{EQ 11})$$

$$= H \cdot S(s) \Big|_{s = \hat{i}_d + \eta \cdot (u + Jv) < s_o} \quad (\text{EQ 12})$$

$$= \eta HJv + H \cdot (\hat{i}_d + \eta u). \quad (\text{switching region}) \quad (\text{EQ 13})$$

In this case the loop gain is ηHJ , so we must have $\eta HJ < 1$ for this to be a stable state. If this is the case, we can solve for device output; we find that

$$x = \frac{PH \cdot (\hat{i}_d + \eta u)}{(1 - \eta HJ)} \quad (\text{switching region—stable}) \quad (\text{EQ 14})$$

If, however, $\eta HJ \geq 1$, the feedback signal increases by a factor of ηHJ on each pass through the feedback loop so that v increases rapidly until the input to the saturating component exceeds s_o and the IBOD enters the ON region. In this case the switching region is an unstable state.

In the on region we have

$$v = T(t) \Big|_{t = H \cdot S(s) > t_o; s > s_o} \quad (\text{EQ 15})$$

$$= H \cdot S(s) \Big|_{s = \hat{i}_d + \eta \cdot (u + Jv) > s_o} \quad (\text{EQ 16})$$

$$= \eta HJBv + Hs_o \cdot (1 - B) + HB \cdot (\hat{i}_d + \eta u). \quad (\text{on region}) \quad (\text{EQ 17})$$

Again we have two cases. Assuming on-region loop gain $\eta HJB < 1$, we find that the output is given by

$$x = \frac{PH \cdot (s_o \cdot (1 - B) + B \cdot (\hat{i}_d + \eta u))}{(1 - \eta HJB)} \quad (\text{on region}) \quad (\text{EQ 18})$$

Note that the saturated output comprises three terms: a constant term, a noise term, and a term linearly proportional to the input.

In the case of loop gain $\eta HJB \geq 1$, the photon flux v and therefore the output x grow without bound. This is an aphysical situation and is largely an artifact of the model we chose for saturation. A more accurate model of saturation would be as in Figure 13, with continuously decreasing incremental gain S' . In this case the on-region loop gain is $\eta HJS'$, and for sufficiently large values of s , S' must approach zero if the device's energy consumption is limited. Thus for sufficiently large s , the on-region loop gain would be forced to values below one.

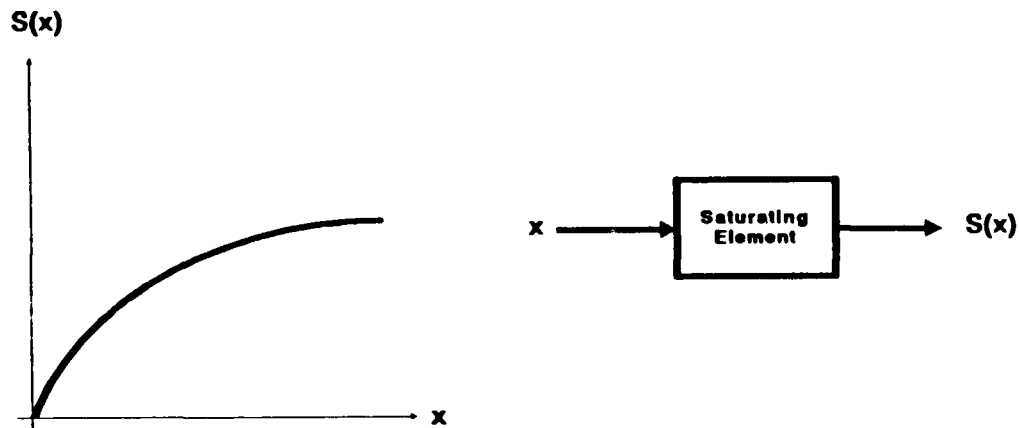


Figure 13. A more realistic model of a saturating element.

Consider now that we can partition the operation of the IBOD model into three modes, based upon the value of the linear gain components. For device parameter values such that $\eta HJ < 1$, the IBOD is stable in all three operating regions, and the output is a unique piecewise linear function of the input as shown in Figure 14a. For $\eta HJ \geq A^{-1}$, only the on region is a stable operating region; the IBOD is always saturated as in Figure 14b. For parameter values such that $1 \leq \eta HJ < A^{-1}$, both the off region and the on region are stable operating regions, but the switching region is unstable. When the device enters the switching region from the off region, the output increases until the device is forced into the on state, as in Figure 14c. This is the bistable operating mode.

Note that this model represents a single independent pixel of the IBOD; crosstalk from adjacent pixels is ignored. Furthermore, we have modelled only the steady-state behavior of the device; this model does not take into account the time- or frequency-dependent behavior of the IBOD.

B. Device Characteristic Measurement Apparatus

In this subsection we describe the apparatus used to measure the input-output characteristic of the IBOD prototypes. Figure 15 shows the apparatus used to trace input-output curves. A tube assembly is used to isolate the device input from external sources and external device output. Mounted to one end of the input isolation tube is the IBOD prototype to be tested. Mounted to the opposite end of the tube is the LED used to produce the input signal. A yellow LED was used for the

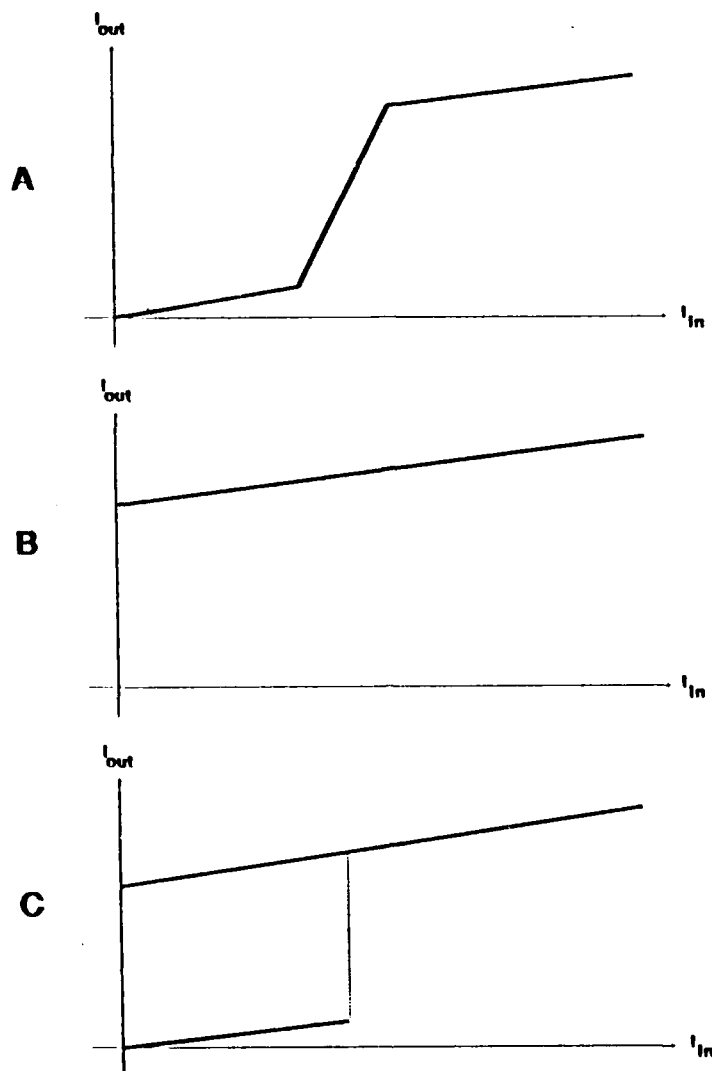


Figure 14. The Three Operating Modes Predicted for the IBOD. A) Piecewise linear amplification mode; B) Saturated mode; C) Bistable mode.

measurements discussed in this report. In the line-of-sight of the LED was a Hamamatsu R980 End-On photomultiplier tube. The PMT was recessed into a well to minimize the effect of feedback light on the received signal at the PMT.

Early tests of the apparatus indicated that light from the IBOD output feeding back through the MCP and photocathode was still sufficiently strong at the PMT to require additional screening, so a protective ridge mask was added on the IBOD side of the PMT well opening to reduce the effect of feedback light on input light measurements. The effect was sufficiently reduced to allow reasonably high SNR measurements of the input intensity from the LED, but the effect can still be detected on input-output characteristic traces at the part of the trace where the IBOD is reset with zero input intensity—note the nonzero PMT signal falling with the output signal when the IBOD is reset in Figure 19.

A United Detector Technologies PIN-10DI p-i-n photodiode detector was mounted to the output face of the IBOD prototype. For some tests the detector abutted the IBOD

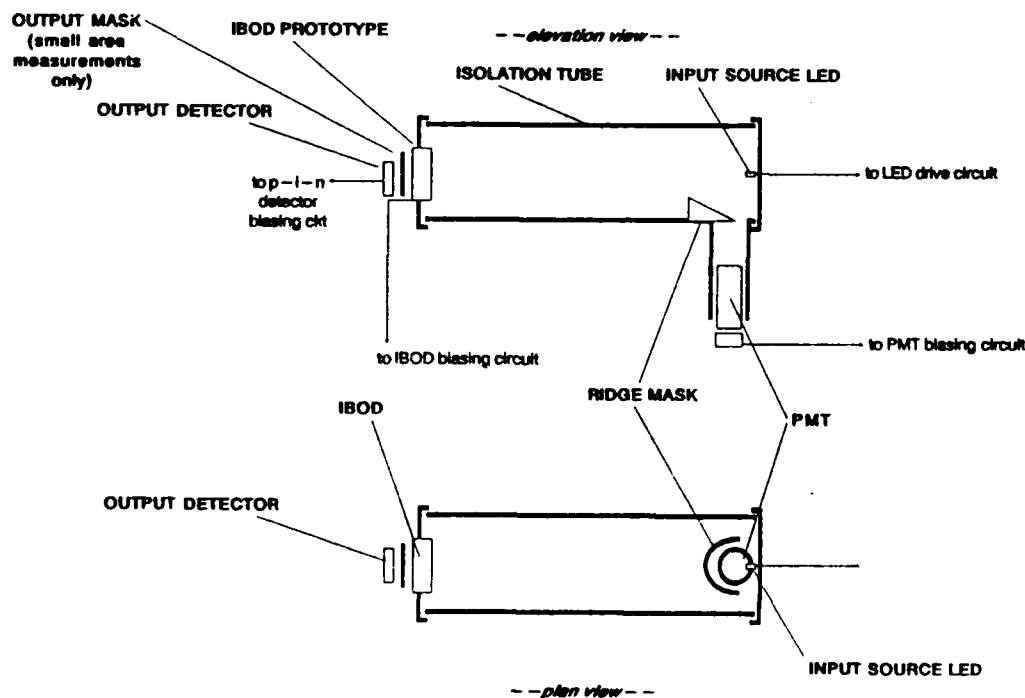


Figure 15. Apparatus Used for Measurement of IBOD Input-Output Characteristic.

output directly so that the output of the detector was proportional to the total intensity output of the IBOD integrated over the entire output area. For other tests the detector abutted a mask covering all but a small area (approximately 1mm diameter) of the IBOD output, so that only the output of a small portion of the IBOD active area was measured. For these tests the input was similarly masked, but the open area was somewhat larger to avoid alignment problems. The open areas of the output mask were not identical from one small-area test to another, so that output values from one small-area test to another are not comparable; the different open areas resulted in integration over different total areas and thus different total measured signal powers for identical intensities. Furthermore, because the smallest signal measurable by the p-i-n detector exceeded the dynamic range of the PMT, it was not possible to link the input and output scales. Thus input and output are each measured linearly, and the input scale used is at a much higher sensitivity than the output scale, but the two cannot be more exactly related.

The p-i-n detector was biased as shown in Figure 16a; the biasing circuit and transconductance amplification circuit for the PMT are shown in Figure 16b. The output voltages are given by

$$v_{pin} = i_{pin} \cdot 10k\Omega; \quad (EQ 19)$$

$$v_{pmt} = i_{pmt} \cdot 100k\Omega \quad (EQ 20)$$

where i_{pin} is the output current of the p-i-n detector and i_{pmt} is the output current of the PMT.

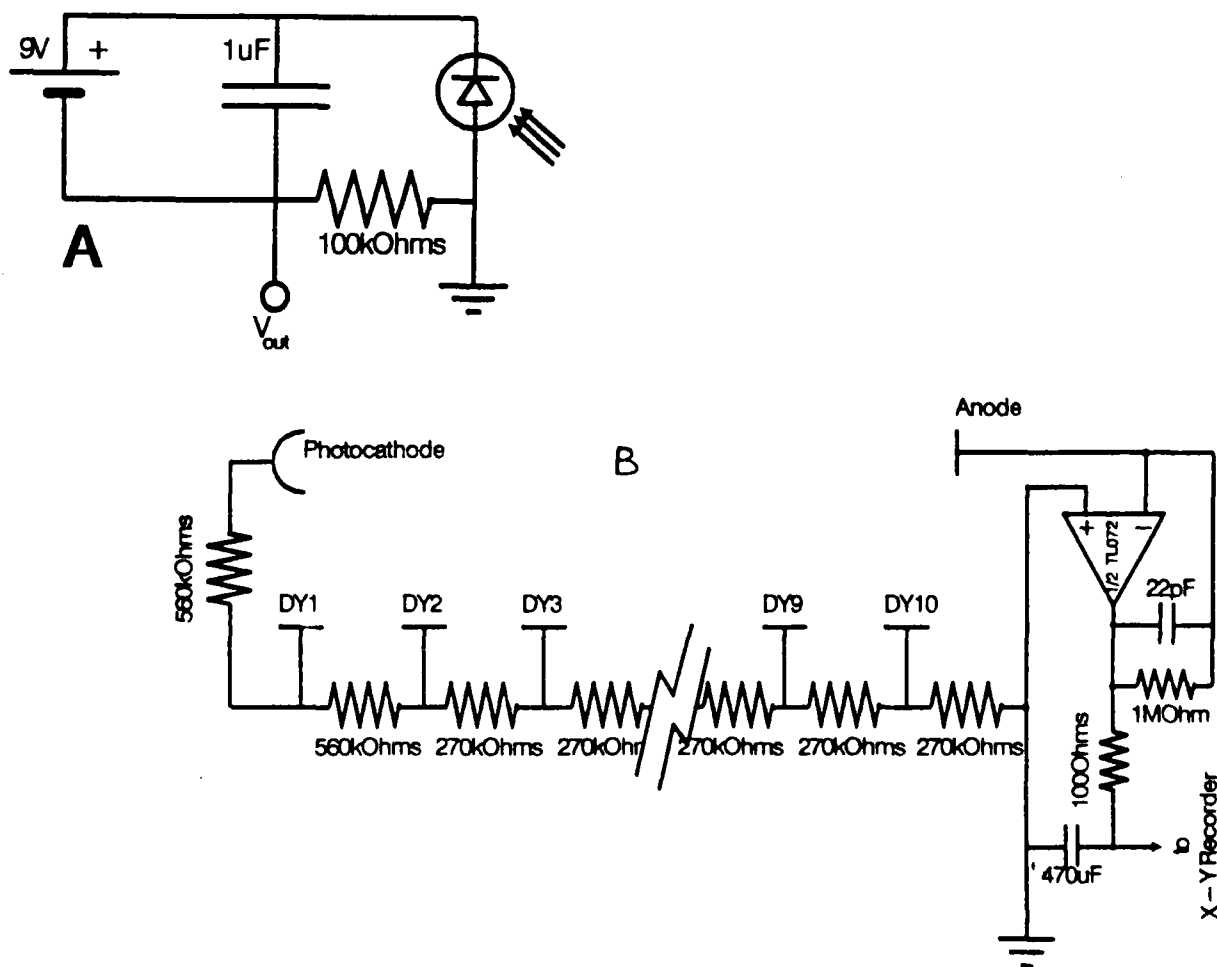


Figure 16. Biasing Circuitry for Detectors used in the IBOD Characteristic Measurement Apparatus. A) P-I-N Diode biasing circuit; B) PMT biasing circuit and transconductance amplifier.

The detector signals were used to drive an HP 7046A X-Y Recorder; the detected input intensity signal from the PMT drove the x input of the recorder, the detected output intensity signal from the p-i-n detector drove the y input. A 470- μ F capacitor across the x input of the recorder was used to filter out noise from the PMT signal.

The LED used to produce the IBOD optical input signal was controlled by the drive circuit illustrated in Figure 17. An integrator circuit provides the driving current to the LED. The input to the integrator is switched manually between the positive and negative rail. The output is thus a ramp in voltage. The time constant associated with the integrator can be varied so that the time required for a ramp from zero to 15V (+rail) can be adjusted. For all the measurements made on the IBOD prototypes, the ramp speed was adjusted so that a sweep from zero to 13 volts required approximately 15 seconds.

The IBOD prototype was wired as indicated in Figure 18. A battery and potentiometer arrangement is used to provide a photocathode bias voltage V_{pc} which can be varied from +66V (forward bias) to -66V (reverse bias). This photocathode bias voltage floats on top of the MCP bias voltage, which is generated by a Bertan

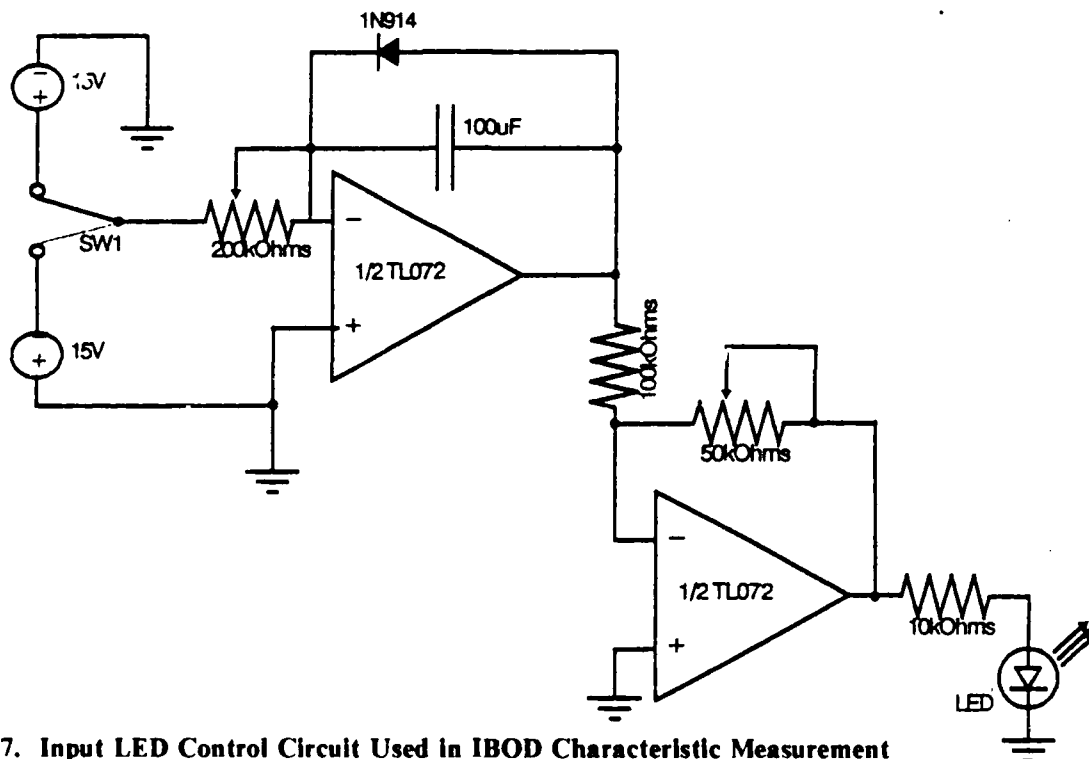


Figure 17. Input LED Control Circuit Used in IBOD Characteristic Measurement Apparatus.

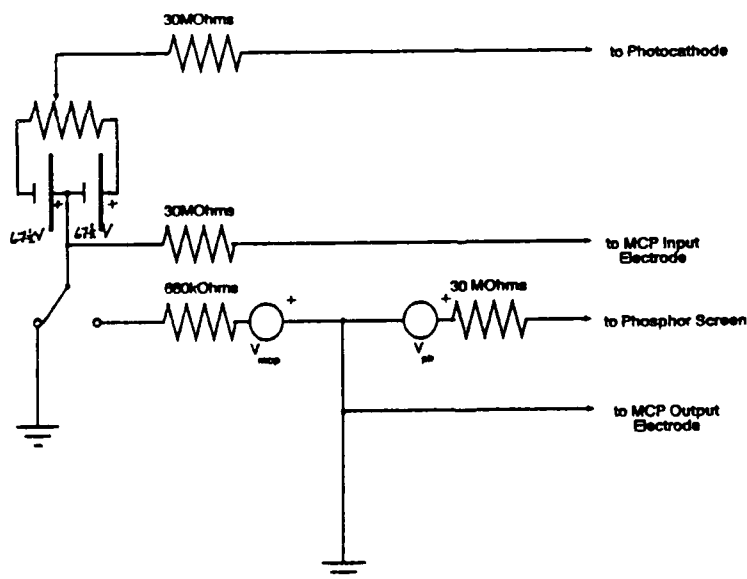


Figure 18. IBOD Prototype Control Circuit Used in IBOD Characteristic Measurement Apparatus.

model 205A-05R variable high-voltage power supply. The MCP bias voltage V_{mcp} is connected to the MCP input electrode through a high-voltage vacuum relay so that the bias can be switched in and out quickly; this provides a direct means of resetting the IBOD once it latches in the ON state. The phosphor screen acceleration potential V_{ph} is applied between the output electrode of the MCP and the phosphor

electrode and is generated by a Glassman model PS/EG-05R-6 variable high-voltage power supply.

C. Device Characteristic Measurement Procedure

In this section we describe both the procedure used to obtain the IBOD characteristic traces and the rationale behind that procedure. The original procedure was modified on two occasions to take into account unexpected behavior observed in the prototypes in the course of testing; we describe here only the procedure in its final form, which was used to generate all the plots discussed in this report.

The curve-tracing apparatus was initially set up with the fifth (final) prototype. The prototype had been aged sufficiently to exhibit bistability before this test began. Once the apparatus had been set up as described above, the various power supplies, biasing circuits, amplifiers and recording equipment were switched on. For all tests discussed in this report the PMT biasing voltage V_{pmt} was set to 800V. Next, the IBOD control biases V_{pc} , V_{mcp} , and V_{ph} were adjusted to obtain a bistable operating point. Let us elaborate.

In early testing it had been observed that the IBOD prototypes exhibited three modes of behavior, in good agreement with the monapixel IBOD model described earlier. That is, for a given set of controlling biases V_{pc} , V_{mcp} , and V_{ph} , the IBOD exhibited one of three behaviors: the device either behaved as a memoryless intensifier of the input signal, remained in the ON state regardless of input, or exhibited bistability. Given that the device behaved as a memoryless intensifier for a particular set of control biases, the device could be forced into the bistable mode by increasing one or more of the biases sufficiently. Once in the bistable mode, the device could be forced back into the memoryless intensifier mode by decreasing one or more of the biases sufficiently, or it could be forced into the perpetual ON mode by increasing one or more of the biases sufficiently. Similarly, the device could be forced back into the bistable mode by decreasing one or more of the biases. Thus the control bias input space of the device is divided into three regions, corresponding to the three behavioral modes.

As a result of this behavior, it was initially necessary to adjust the control biases to find a bistable operating point before bistable operating characteristics could be traced. Once an initial operating point had been found, control biases could be varied about this point and traces made of the resulting input-output characteristics of the IBOD. Control biases were not varied sufficiently to force the IBOD out of the bistable mode, however, since the purpose of this series of measurements was to explore the bistable characteristic. The procedure used to make a trace of the input-output characteristic for a given set of control biases is described below.

With the IBOD controlling biases set to their desired values for a particular trace, the MCP relay was activated, switching in the MCP bias voltage. Next the recorder pen was dropped and the input sweep generator set to slowly increase the optical input signal into the IBOD. Once the input signal had reached the upper limit of its sweep or the IBOD output had changed state, the input sweep generator was set to slowly decrease the input signal. At the end of the sweep, the MCP was switched off and the recorder pen raised.

The first few input-output traces obtained demonstrated an unexpected behavior in the IBOD which required a change in the measurement procedure. Figure 19 illustrates the problem. The traces of Figure 19 were made according to the procedure described above. The traces were made in the order in which they are numbered. The time between each trace and the previous trace is indicated in the accompanying table; prior to the first trace, the device had not been activated for at least eight hours. Note that the control biases are identical for every trace in this set. Indeed, the only difference in the traces is the time at which each trace was made. Note the shift of the threshold to lower and lower values with consecutive traces until trace 7, when the device was allowed a five-minute rest. This trace set indicates a strong dependence of the input-output characteristic upon recent history of the device. To obtain meaningful data, it was necessary to find a means of overcoming this dependence.

It was determined after additional testing that the device input-output characteristic was relatively stable and consistent for measurements made at regular intervals once a steady state was attained. A five-minute resting period was thus adopted between successive traces. That is, the device was allowed a recovery period of five minutes between the end of one trace and the beginning of the next trace for all trace sets. In addition, before any usable data was taken, warm-up traces were taken at five-minute intervals until the device reached steady state.

Two types of measurements were made on the fifth prototype: integrated-area measurements and small-area measurements. For integrated-area measurements, the output detector was abutted directly to the IBOD output so that the indicated output signal in the traces so labelled represents the output intensity of the IBOD integrated over the entire active area of the device. For small-area measurements, a mask exposing only a small area of the IBOD output (approximately 1-2 mm diameter) was employed between the IBOD output and the output detector, so that the indicated output signal in traces so labelled represents the output intensity integrated over the area exposed by the mask. Another mask was attached to the corresponding area of the input face of the IBOD. The purpose of the small-area measurements was to obtain characteristic measurements for independent areas of the output. Since pixel blooming made this impossible under normal circumstances, the masks were developed to obtain independent behavior of different areas of the IBOD. We digress.

The pixel blooming behavior of the IBOD could be easily observed when an input very near (but slightly above) the switching threshold of the device was applied to the IBOD. When exposed to such an input, one small area of the output would turn on first, and the active area of the output would spread to surrounding areas until the entire bistable of the device was active. The seed area which initially turned on we termed the primary hot spot. If the input area corresponding to the primary hot spot were covered so that it was masked from all input and the same input were applied to the device, a new area became the first area of the output to turn on and served as the new seed from which the turned-on area grew. Similarly, if the input corresponding to this secondary hot spot were covered, a tertiary hot spot appeared. Thus measurements could be obtained for independent areas of the IBOD output by masking off the input area corresponding to the primary hot spot and placing a mask over the IBOD output so that the output detector was exposed only to the secondary hot spot.

TRACE #	V _{pc}	V _{mcp}	V _{ph}	ELAPSED TIME SINCE LAST TRACE
---------	-----------------	------------------	-----------------	----------------------------------

1	30V	700V	2.4kV	-first trace-
2	30V	700V	2.4kV	10 sec
3	30V	700V	2.4kV	10 sec
4	30V	700V	2.4kV	20 sec
5	30V	700V	2.4kV	30 sec
6	30V	700V	2.4kV	40 sec
7	30V	700V	2.4kV	10 sec
8	30V	700V	2.4kV	0 sec

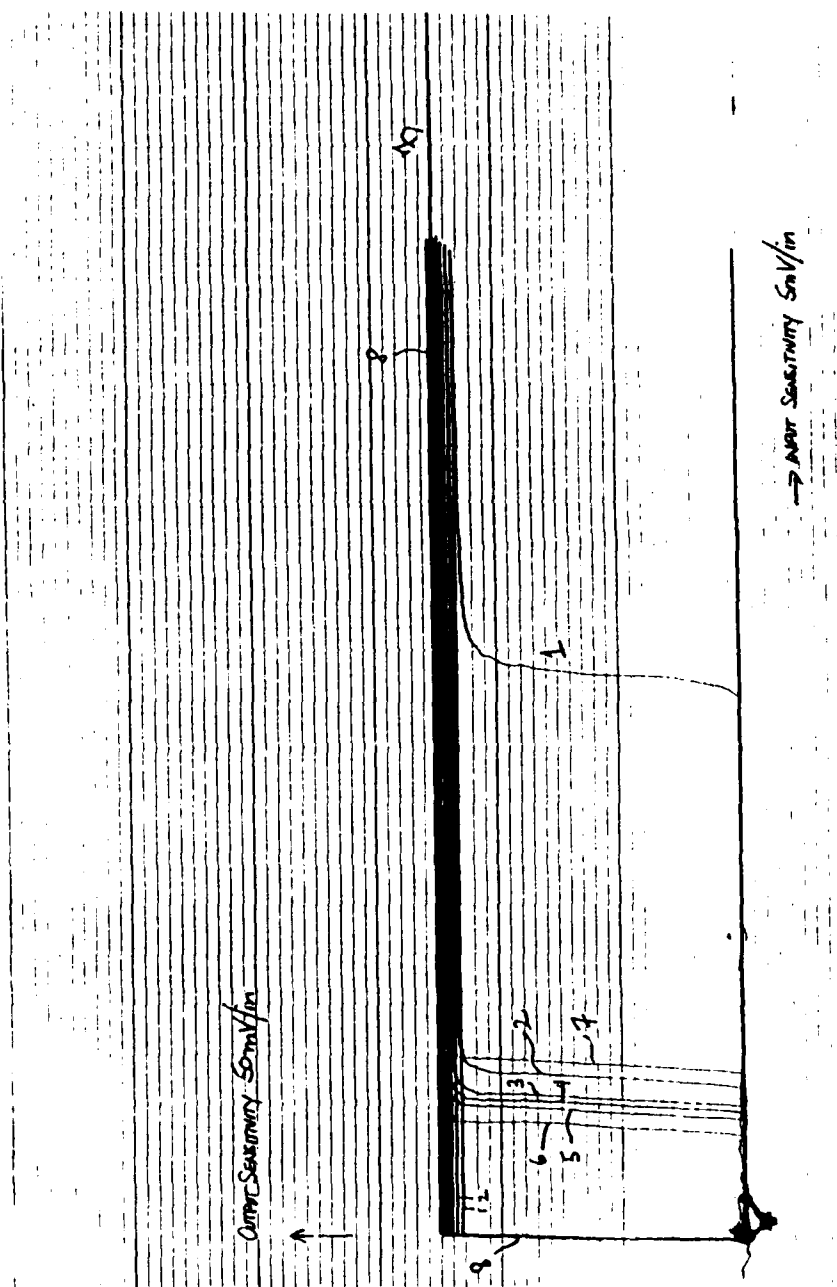


Figure 19. First Trace Set of Input-Output Curve of IBOD Showing Temporal Instability.

D. Experimental Results

A total of eight integrated-area trace sets were made of the input-output characteristic of the fifth prototype. The first three were used to determine the sufficiency of the five-minute relaxation period; one of these appears in Figure 19. In three of the following trace sets, two of the IBOD control biases were held fixed and the third was varied as a parameter as several traces were made. Figure 20 shows the trace set for which V_{mcp} and V_{ph} were held fixed and V_{pc} was varied as a parameter. Figure 21 shows the trace set for which V_{mcp} and V_{pc} were held fixed and V_{ph} was varied as a parameter; and Figure 22 shows the trace set for which V_{pc} and V_{ph} were held fixed and V_{mcp} was varied.

Six small-area trace sets were made of the input-output characteristic of the fifth prototype. The first three trace sets show the characteristic measured for the primary hot spot with each of the three control biases varied as parameters while the other two biases are fixed; the second three trace sets similarly show the characteristic measured for the secondary hot spot of the fifth prototype. These trace sets appear in Figures 23 through 28. Note that, while input scales of these plots are identical, the output scales differ between the primary and secondary hot spot measurements due to differing output mask areas.

A single small-area trace set was made of the input-output characteristic of the fourth prototype. This trace set is shown in Figure 29. Note the similarity in behavior to the fifth prototype.

E. Analysis of Results

In this section we analyze the important observations and measurements of IBOD behavior described in the previous sections and compare that behavior with the model's predictions. We divide the discussion into three parts: first we discuss the observed resolution problem, next the unexpected temporal dependence of the input-output characteristic, and finally the control bias dependencies of the characteristic.

1. Resolution

As the monapixel IBOD model concerns only the behavior of a single pixel of the device, the issue of pixel blooming is outside the scope of the model. Thus we briefly discuss the nature of the crosstalk-induced pixel-blooming problem here.

The resolution of the second generation image intensifier is quite high, typically on the order of 30-40lp/mm. Unfortunately the feedback mechanism which makes bistability possible also makes the IBOD much more sensitive to crosstalk from pixel to pixel (with each pore of the MCP representing a pixel). Figure 30 illustrates the occurrence of crosstalk both on the IBOD architecture and on the IBOD model. Because of this crosstalk, a pixel with input below the threshold intensity might be forced into the ON state by crosstalk from adjacent pixels. For this reason the IBOD architecture includes pixel confinement layers to reduce crosstalk. Studies on the optical transmission characteristics of the MCP (see Appendix) showed a selectivity in the transmission of the MCP for light propagating along the bias angle of the MCP parallel to the channels. Thus for sufficiently low linear

TRACE #	V_{pc}	V_{mcp}	V_{ph}	ELAPSED TIME SINCE LAST TRACE
1	28V	700V	2.4kV	~7 min
2	28V	700V	2.4kV	5 min
3	24V	700V	2.4kV	5 min
4	20V	700V	2.4kV	5 min
5	16V	700V	2.4kV	5 min
6	32V	700V	2.4kV	5 min
7	36V	700V	2.4kV	5 min
8	40V	700V	2.4kV	5 min
9	44V	700V	2.4kV	5 min
10	48V	700V	2.4kV	5 min
11	52V	700V	2.4kV	5 min

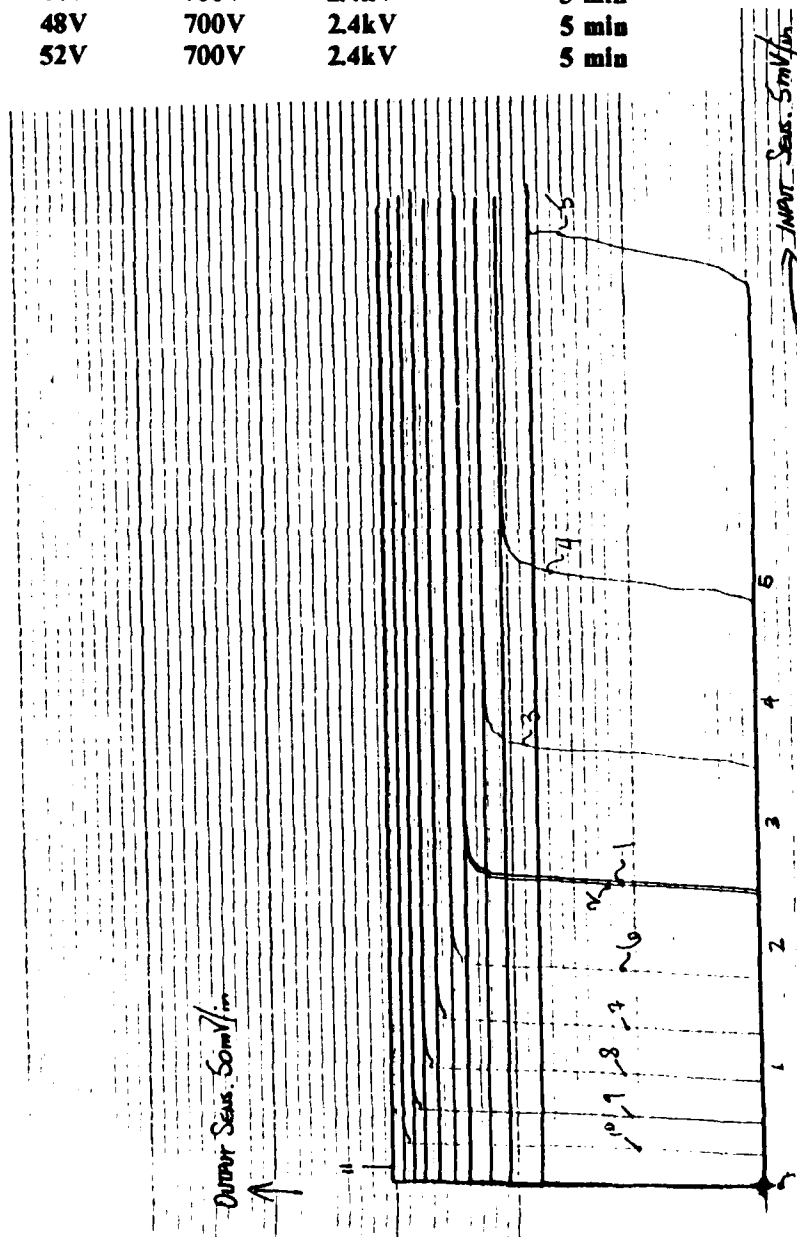


Figure 20. Input-Output Characteristic of Fifth IBOD Prototype with V_{mcp} and V_{ph} Held Fixed and V_{pc} Varied as a Parameter.

TRACE #	V_{pc}	V_{mcp}	V_{ph}	ELAPSED TIME SINCE LAST TRACE
1	28V	700V	2.4kV	-7 min
2	28V	700V	2.4kV	5 min
3	28V	700V	2.4kV	5 min
4	28V	700V	2.2kV	5 min
5	28V	700V	2.3kV	5 min
6	28V	700V	2.35kV	5 min
7	28V	700V	2.45kV	5 min
8	28V	700V	2.5kV	5 min
9	28V	700V	2.6kV	5 min
10	28V	700V	2.65kV	5 min

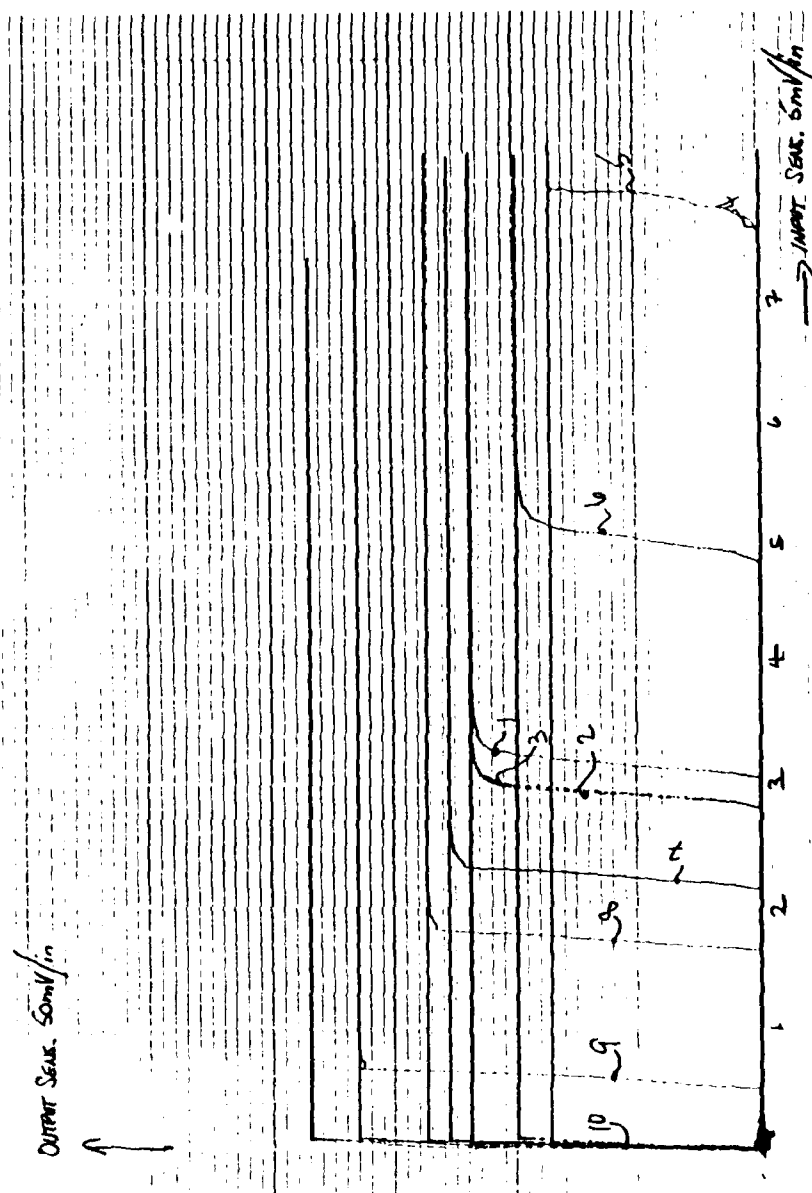


Figure 21. Input-Output Characteristic of Fifth IBOD Prototype with V_{mcp} and V_{pc} Held Fixed and V_{ph} Varied as a Parameter.

TRACE #	V_{pc}	V_{mcp}	V_{ph}	ELAPSED TIME SINCE LAST TRACE
1	28V	700V	2.4kV	~5 min
2	28V	700V	2.4kV	5 min
3	28V	700V	2.4kV	5 min
4	28V	701V	2.4kV	5 min
5	28V	702V	2.4kV	5 min
6	28V	704V	2.4kV	5 min
7	28V	706V	2.4kV	5 min
8	28V	710V	2.4kV	5 min
9	28V	714V	2.4kV	5 min
10	28V	718V	2.4kV	5 min
11	28V	696V	2.4kV	5 min
12	28V	698V	2.4kV	5 min

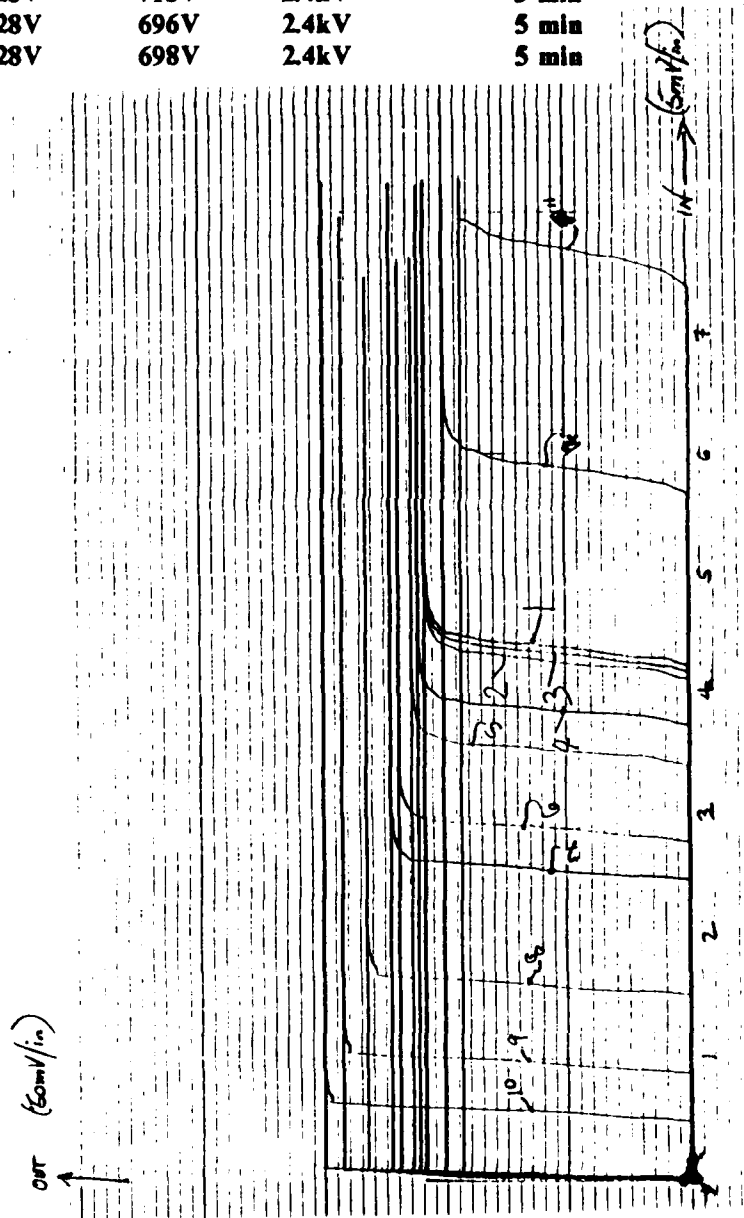


Figure 22. Input-Output Characteristic of Fifth IBOD Prototype with V_{pc} and V_{ph} Held Fixed and V_{mcp} Varied as a Parameter.

TRACE #	V _{pc}	V _{mcp}	V _{ph}	ELAPSED TIME SINCE LAST TRACE
1	28V	700V	2.4kV	-first trace-
2	28V	700V	2.4kV	3 min
3	28V	700V	2.4kV	5 min
4,5,6	28V	700V	2.4kV	5 min
7	24V	700V	2.4kV	5 min
8	26V	700V	2.4kV	5 min
9	32V	700V	2.4kV	5 min
10	36V	700V	2.4kV	5 min
11	44V	700V	2.4kV	5 min
12	50V	700V	2.4kV	5 min

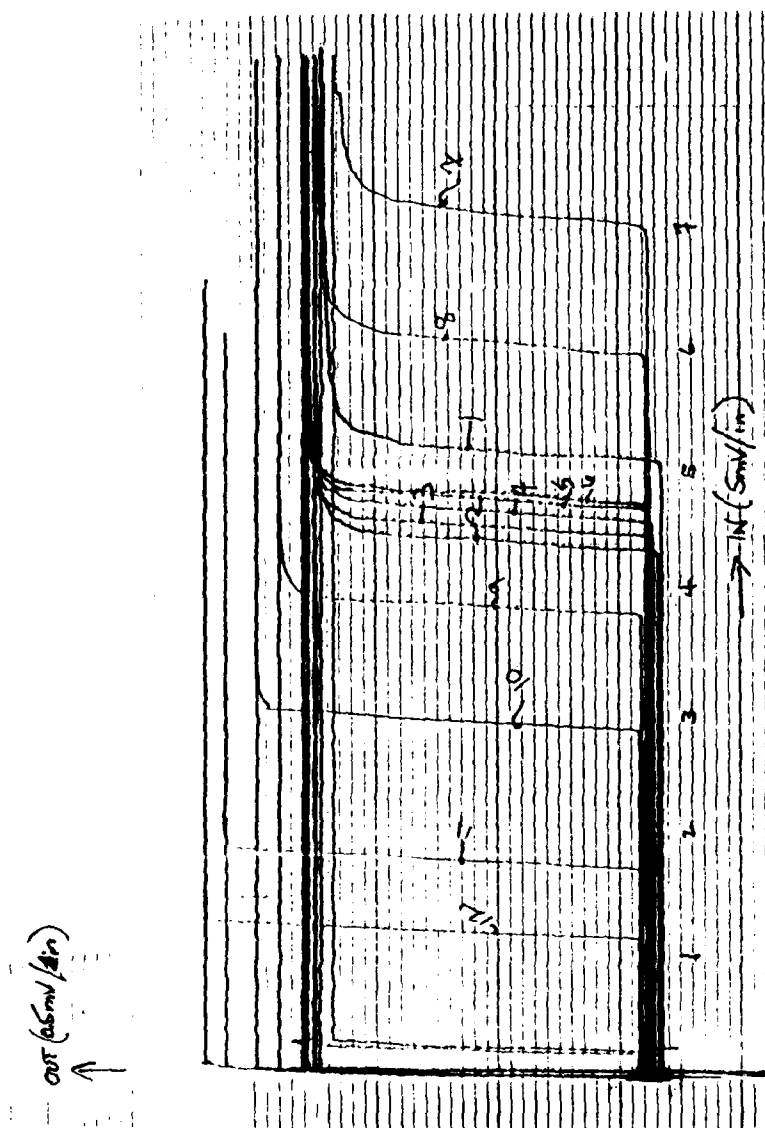


Figure 23. Fifth Prototype IBOD Input-Output Curve for Primary Hot Spot with V_{mcp} and V_{ph} Fixed and V_{pc} Varied as a Parameter. Note that for these traces the PIN detector bias resistor value was changed from 100kΩ to 1MΩ.

TRACE #	V_{pc}	V_{mcp}	V_{ph}	ELAPSED TIME SINCE LAST TRACE
1	28V	700V	2.4kV	~5 min
2	28V	700V	2.4kV	5 min
3	28V	700V	2.45kV	5 min
4	28V	700V	2.6kV	5 min
5	28V	700V	2.35kV	5 min
6	28V	700V	2.2kV	5 min

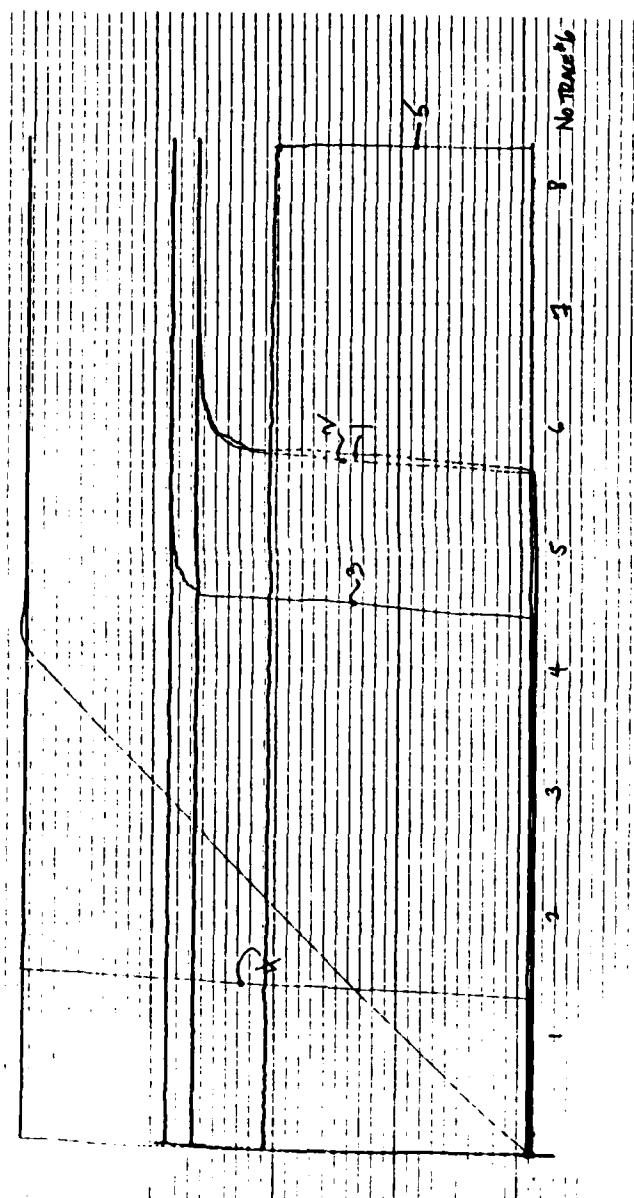


Figure 24. Fifth Prototype IBOD Input-Output Curve for Primary Hot Spot with V_{mcp} and V_{pc} Fixed and V_{ph} Varied as a Parameter. Note that for these traces the PIN detector bias resistor value was changed from 100k Ω to 1M Ω .

TRACE #	V_{pc}	V_{mcp}	V_{ph}	ELAPSED TIME SINCE LAST TRACE
1	28V	700V	2.4kV	~5 min
2	28V	700V	2.4kV	5 min
3	28V	700V	2.4kV	5 min
4	28V	700V	2.4kV	5 min
5	28V	705V	2.4kV	5 min
6	28V	710V	2.4kV	5 min
7	28V	715V	2.4kV	5 min
8	28V	695V	2.4kV	5 min
9	28V	698V	2.4kV	5 min

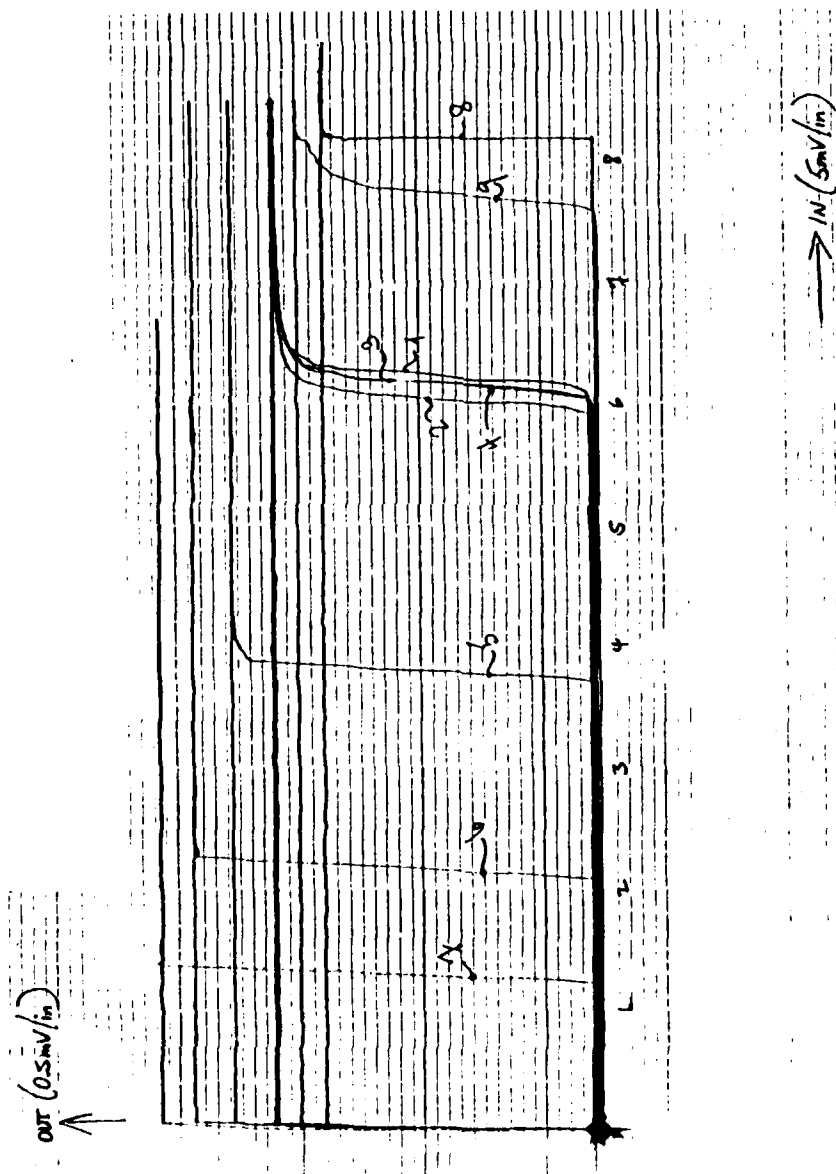


Figure 25. Fifth Prototype IBOD Input-Output Curve for Primary Hot Spot with V_{pc} and V_{ph} Fixed and V_{mcp} Varied as a Parameter. Note that for these traces the PIN detector bias resistor value was changed from 100k Ω to 1M Ω .

TRACE #	V_{pc}	V_{mcp}	V_{ph}	ELAPSED TIME SINCE LAST TRACE
1	28V	700V	2.4kV	-10 min
2	28V	700V	2.4kV	5 min
3	32V	700V	2.4kV	5 min
4	32V	700V	2.4kV	5 min
5	36V	700V	2.4kV	5 min
6	36V	700V	2.4kV	5 min
7	44V	700V	2.4kV	5 min
8	50V	700V	2.4kV	5 min

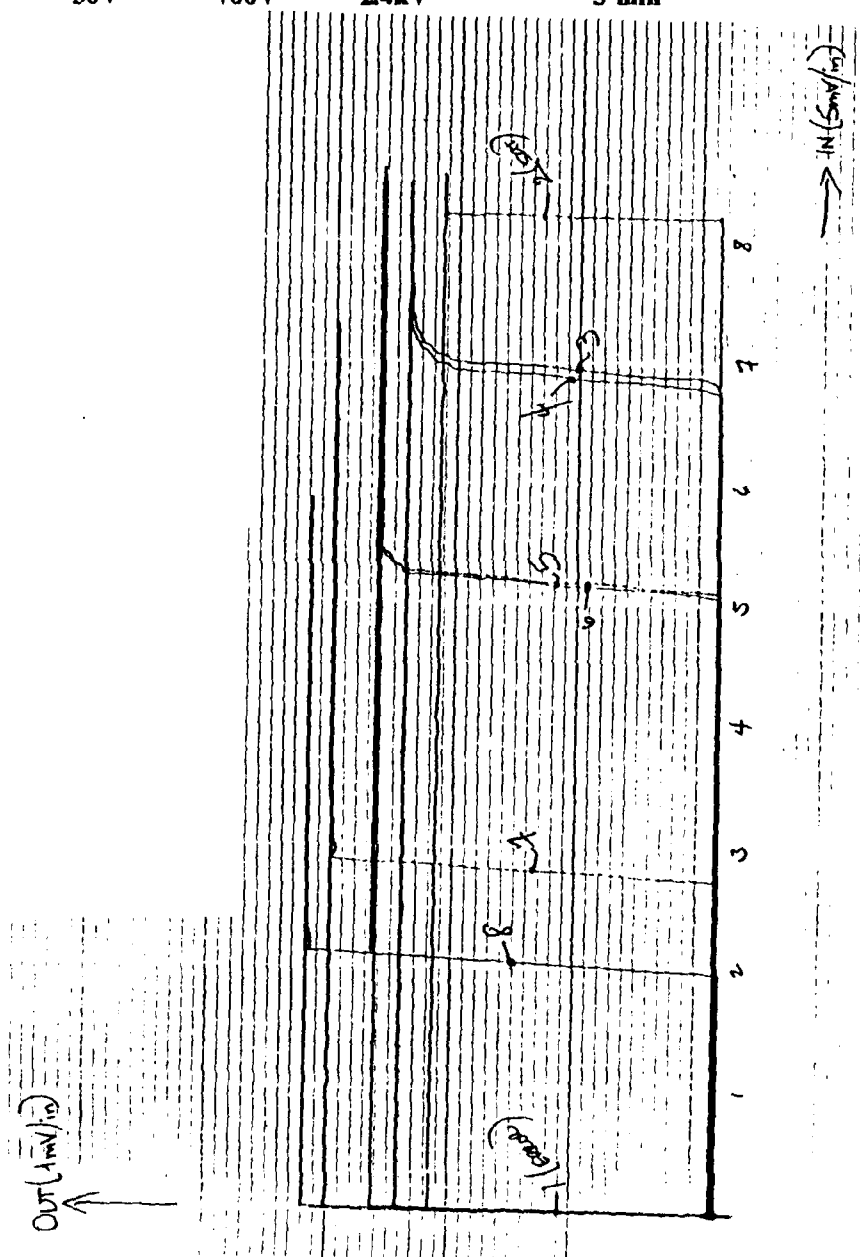


Figure 26. Fifth Prototype IBOD Input-Output Curve for Secondary Hot Spot with V_{mcp} and V_{ph} Fixed and V_{pc} Varied as a Parameter. Note that for these traces the PIN detector bias resistor value was changed from 100k Ω to 1M Ω .

TRACE #	V_{pc}	V_{mcp}	V_{ph}	ELAPSED TIME SINCE LAST TRACE
1	36V	700V	2.4kV	~5 min
2	36V	700V	2.4kV	5 min
3	36V	700V	2.5kV	5 min
4	36V	700V	2.3kV	5 min
5	36V	700V	2.35kV	5 min

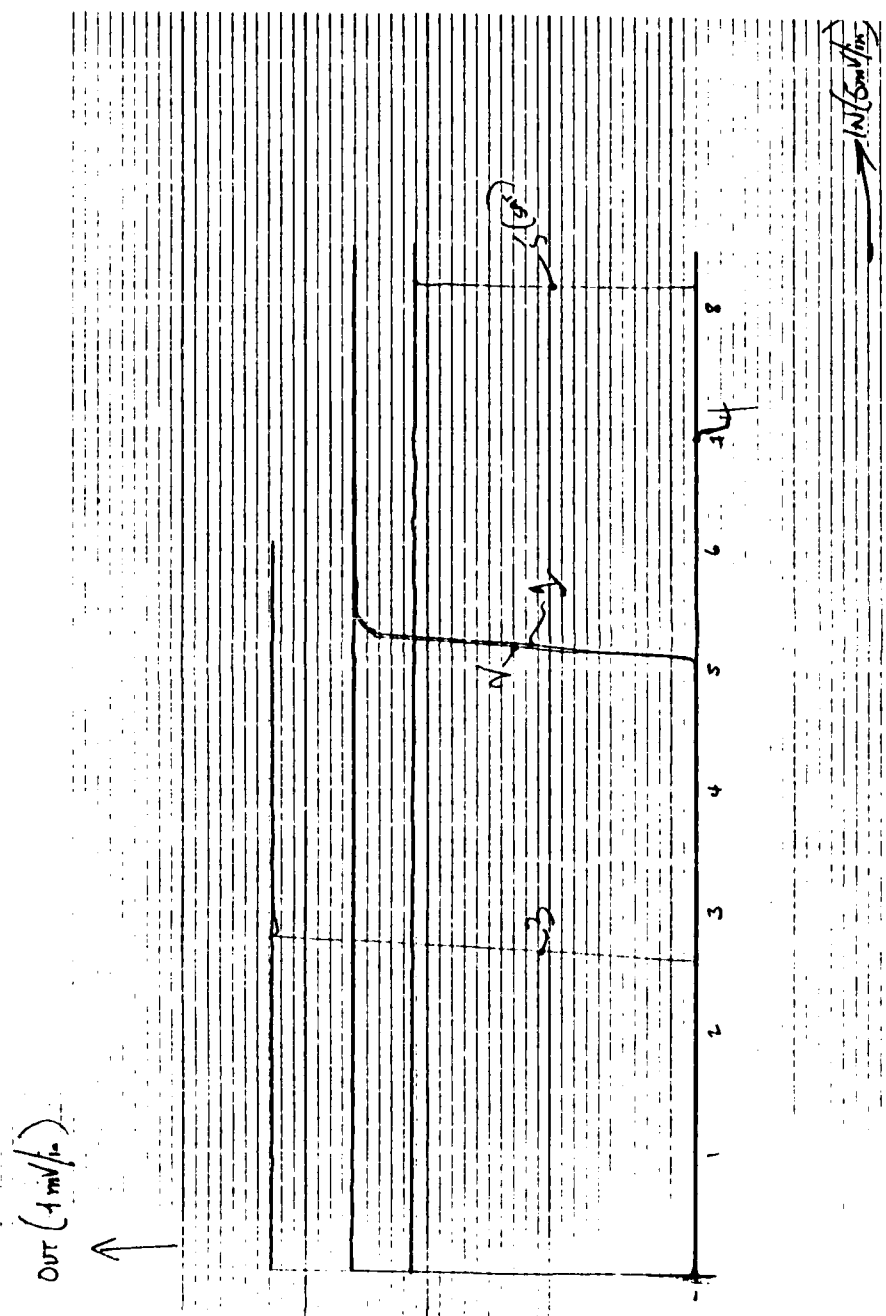


Figure 27. Fifth Prototype IBOD Input-Output Curve for Secondary Hot Spot with V_{mcp} and V_{pc} Fixed and V_{ph} Varied as a Parameter. Note that for these traces the PIN detector bias resistor value was changed from 100k Ω to 1M Ω .

TRACE #	V_{pc}	V_{mcp}	V_{ph}	ELAPSED TIME SINCE LAST TRACE
1	36V	700V	2.4kV	~5 min
2	36V	700V	2.4kV	5 min
3	36V	710V	2.4kV	5 min
4	36V	698V	2.4kV	5 min
5	36V	705V	2.4kV	5 min

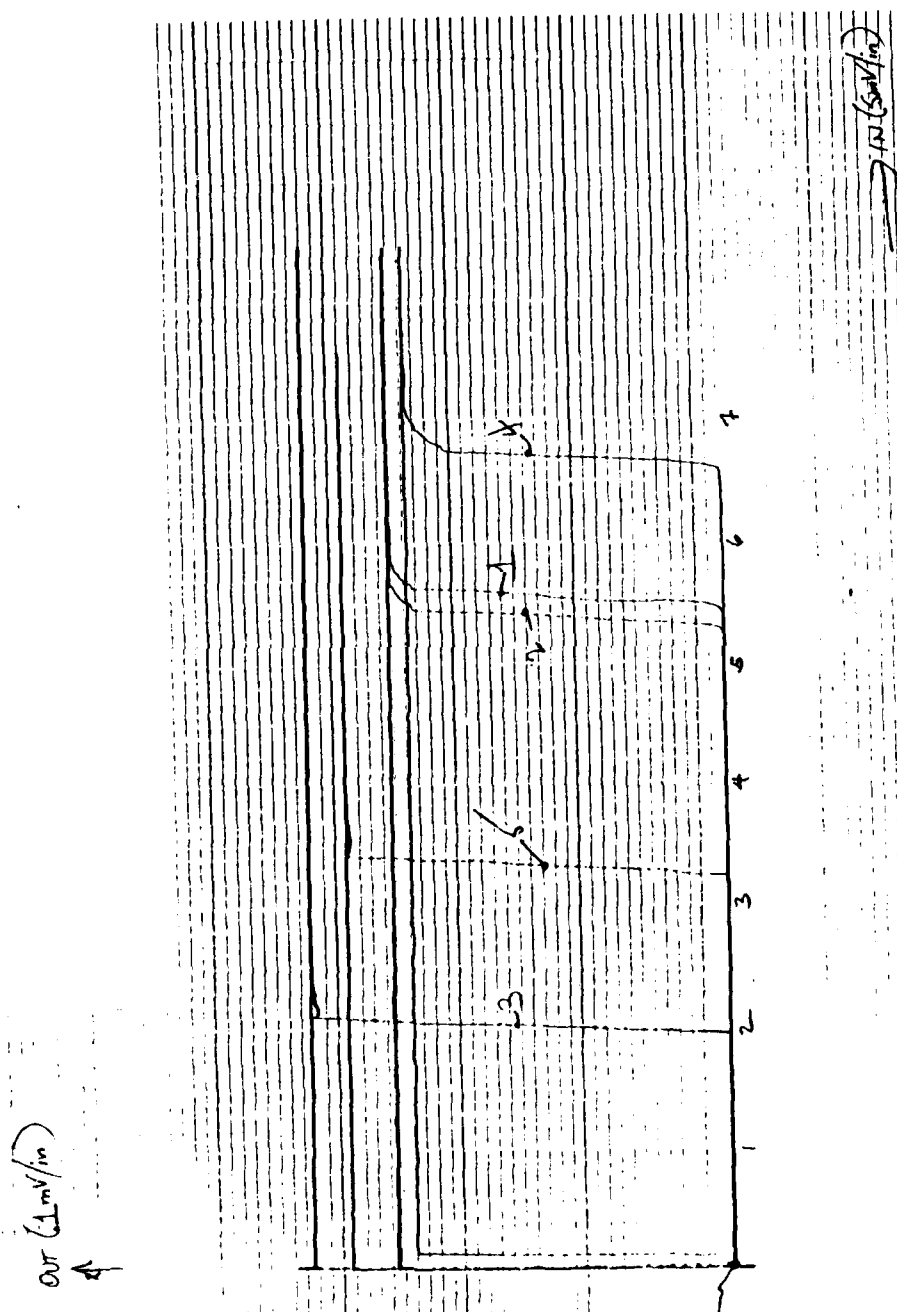


Figure 28. Fifth Prototype IBOD Input-Output Curve for Secondary Hot Spot with V_{ph} and V_{pc} Fixed and V_{mcp} Varied as a Parameter. Note that for these traces the PIN detector bias resistor value was changed from 100k Ω to 1M Ω .

TRACE #	V _{pc}	V _{mcp}	V _{ph}	ELAPSED TIME SINCE LAST TRACE
1	38V	735V	2.65kV	~5 min
2	34V	735V	2.65kV	5 min
3	26V	735V	2.65kV	5 min
4	38V	725V	2.65kV	5 min
5	38V	720V	2.65kV	5 min
6	38V	735V	2.6kV	5 min
7	38V	735V	2.5kV	5 min

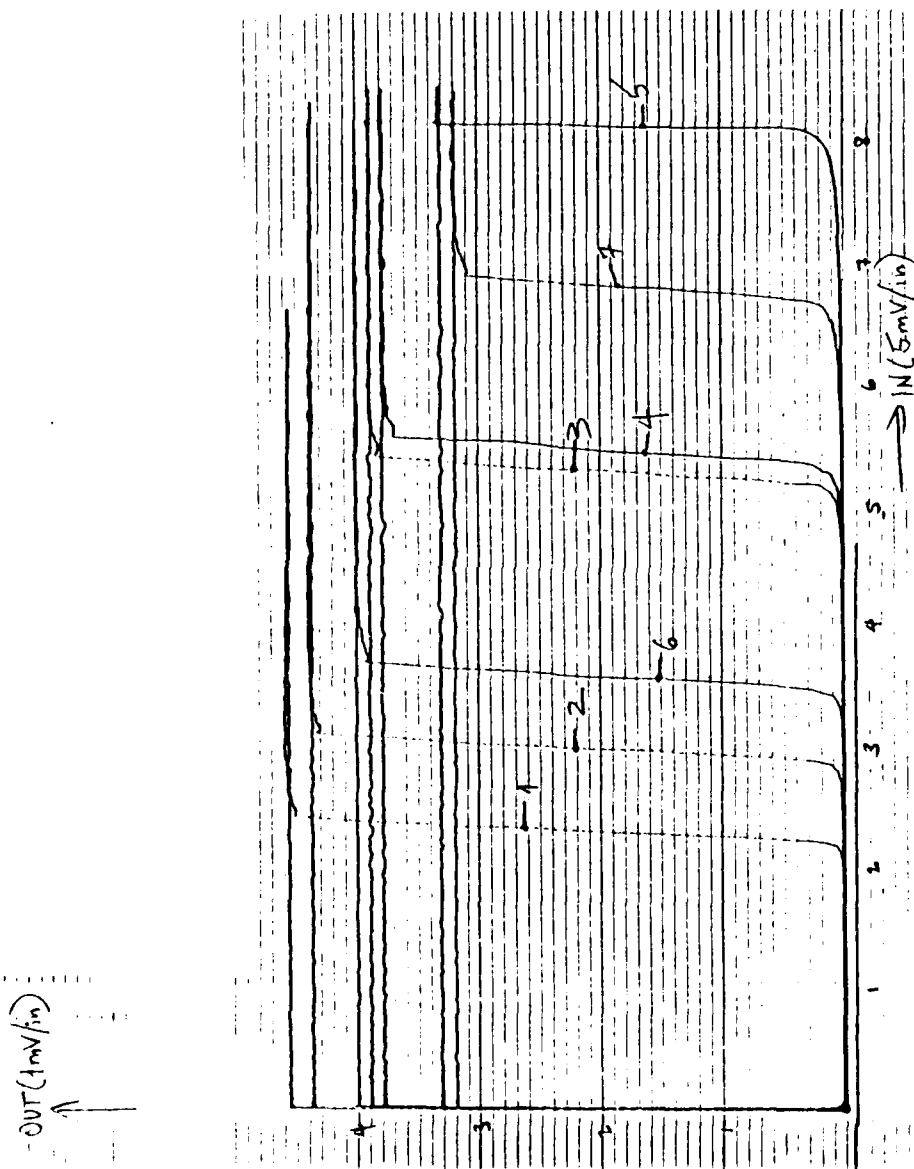


Figure 29. Fourth Prototype IBOD Input-Output Curves for Primary Hot Spot with Variable Parameters. Note that for these traces the PIN detector bias resistor value was changed from 100k Ω to 1M Ω .

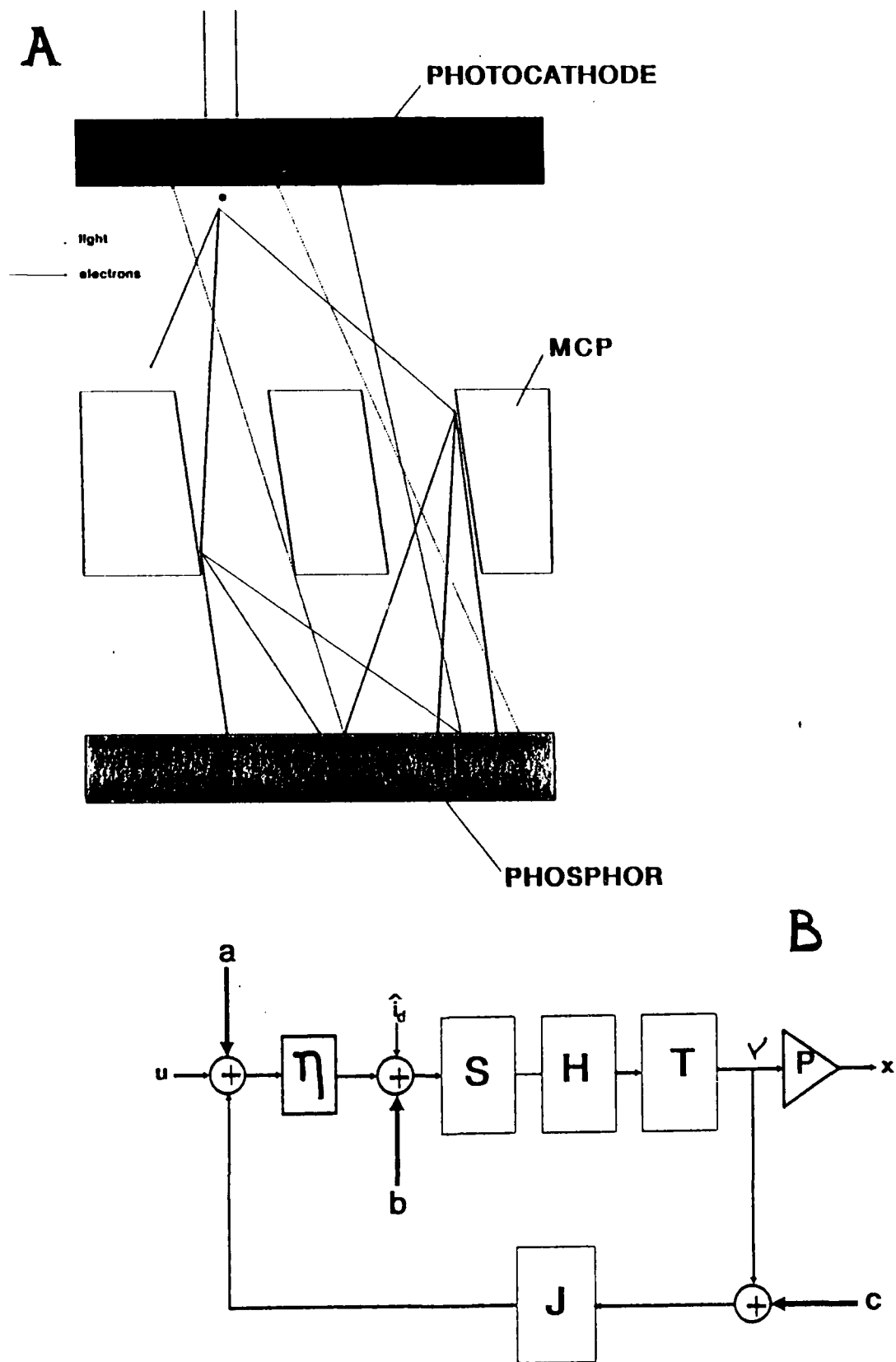


Figure 30. Crosstalk Locations in A) the IBOD Architecture and B) the Monopixel IBOD Model.

component gain values, optical crosstalk could be reduced sufficiently by the MCP's selectivity to significantly reduce blooming. The MCP's selectivity is made more effective by reducing component spacing, but this increases the likelihood of internal arcing, so spacing cannot be reduced arbitrarily.

As can be seen from Figure 30 and inferred from Equation EQ-10, even at reduced levels insufficient to cause blooming, the crosstalk will effectively add to the total noise intensity at a particular pixel, reducing the input intensity required to switch the pixel. As a result, even levels of crosstalk below threshold can significantly effect the input threshold, so that a pixel surrounded by pixels in the ON state would be turned on by a much smaller input signal than a pixel surrounded by pixels in the OFF state. Thus it is important for both resolution and pixel independence that crosstalk be reduced as much as possible.

The behavior observed in the fourth and fifth prototypes demonstrates the problem well. Due to some small nonuniformity in the gains of the various components, the switching threshold is smaller for one small area of the device than for any other part of the active area. When the input of the IBOD is uniformly illuminated, this area switches on first. Crosstalk from this activated area to adjacent pixels causes the activated area to grow until the entire output of the IBOD is turned on. Thus the thresholds of the integrated-area measurements are actually determined by the primary hot spot. When the primary hot spot is masked off from the input, the portion of the device with the smallest switching threshold of the unmasked areas becomes the new hot spot.

As witnessed from the blooming behavior of the two prototypes, the MCP's optical selectivity is inadequate to prevent blooming at the component spacings used, though the reduced spacing of the fifth prototype does appear to reduce the rate of blooming somewhat. Nevertheless, even with total elimination of optical crosstalk, there still exists electron crosstalk between pixels, as electron trajectories cannot be perfectly controlled to align with the MCP channels. As explained above, even when reduced to levels insufficient to induce blooming, inter-pixel crosstalk reduces the operational independence of adjacent pixels. Thus it is desirable to reduce crosstalk as much as possible.

2. Temporal Dependence

The unexpected dependence of input threshold intensity and, to a lesser extent, the saturation intensity of the device, on temporal proximity to device ON time, as documented in Figure 19, required the modification of the characteristic measurement procedure as described previously. Unfortunately the dependence represents an undesirable characteristic of the IBOD prototypes.

Careful observation of the phenomenon indicated that the important parameters were elapsed time since last phosphor screen activation and duration of that activation. We currently have three theories as to the cause. The first is extended decay time of the phosphor. This seems unlikely, however, as the observed effective period of the dependence is several minutes, and the phosphor decay time constant for the P20 phosphor is on the order of a second. A second possible culprit is thermal heating of the phosphor, inducing a variation in phosphor efficiency. Our final theory involves trapping of charge in the phosphor layer requiring a long relaxation time. None of these theories were tested, however, and there are other possible causes.

development program.

3. Control Bias Dependencies

Recall that the monapixel IBOD model accurately predicted the three modes of IBOD behavior. The IBOD model, however, described behavior in terms of component gains rather than bias voltages. In order to compare the behavior observed in the prototypes with that predicted by the monapixel model, then, we need to specify the relationships between control biases and the component gains. Figure 31a shows the a plot of current gain of a MCP vs. MCP bias voltage. Note that the logarithm of MCP gain is essentially proportional to the logarithm of MCP bias voltage. Figure 31b shows the relationship between photocathode bias voltage and luminous sensitivity of the photocathode. Note that for fixed spectrum of the input intensity, the luminous sensitivity is to some degree proportional to the quantum efficiency. Figure 31c shows a plot of luminous output of a phosphor screen vs. phosphor screen accelerating potential. For this plot phosphor with aluminum electrode was used; hence the curve is shifted to more positive potentials by the potential required for electrons to penetrate the aluminum electrode. For the IBODs tested, the curve should be shifted to somewhat lower potentials. For fixed spectral distribution of the output, the luminous output plotted in Figure 31c is proportional to the number of photons emitted by the phosphor; the relationship between photon count and screen potential is thus the essentially linear.

Using this approximate knowledge of the relationship between the gain of the various components and the control bias voltages, we see that the observed modal behavior of the IBOD agrees completely with that predicted by the model. That is, increasing bias voltages correspond to increasing component gains, and the model successfully predicted that as linear component gain was increased from zero the device would go from the memoryless intensification mode to the bistable mode to the perpetual-ON mode. Let us consider the bistable behavior measured in the prototypes and predicted by the model in greater detail.

Note from the trace sets of the previous section that the input-output characteristic can largely be described by two parameters, the input intensity threshold and the output saturation intensity. Figures 32 and 33 show the measured variation of input threshold intensity and of output saturation intensity with MCP bias voltage, respectively. Using the relationship⁷

$$G_{mcp} = \left(\frac{V_{mcp}}{ca} \right)^{\alpha/4} \quad (EQ 21)$$

where G_{mcp} is MCP gain, α is MCP channel-length-to-diameter ratio, and c is a constant with a value of about 10 for scrubbed plates, we can relate MCP bias voltage to MCP gain and therefore to the forward gain H of the IBOD model. Assuming an α of 22, the IBOD model predicts the relationship between IBOD threshold intensity and MCP bias potential depicted in Figure 34. Similarly the model predicts a relationship between the IBOD saturation intensity and MCP bias potential like that depicted in Figure 35.

The curves cannot be compared absolutely, as there are too many parameters of the model which can be varied, but the general shapes of the predicted curves can be

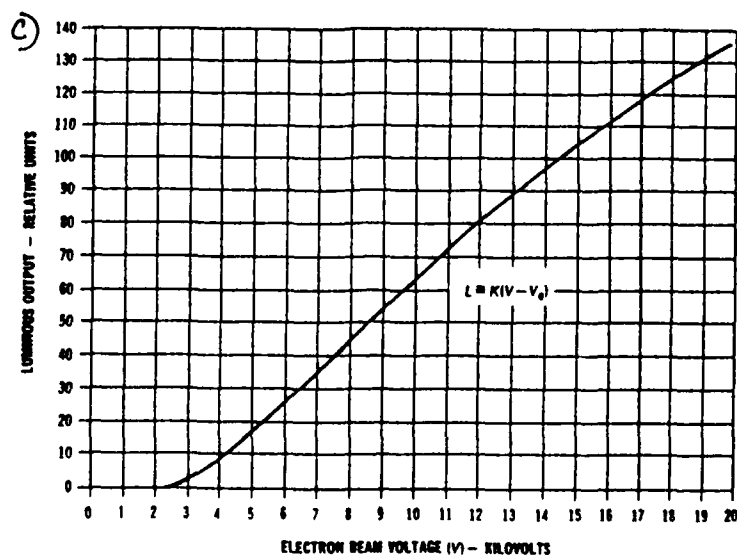
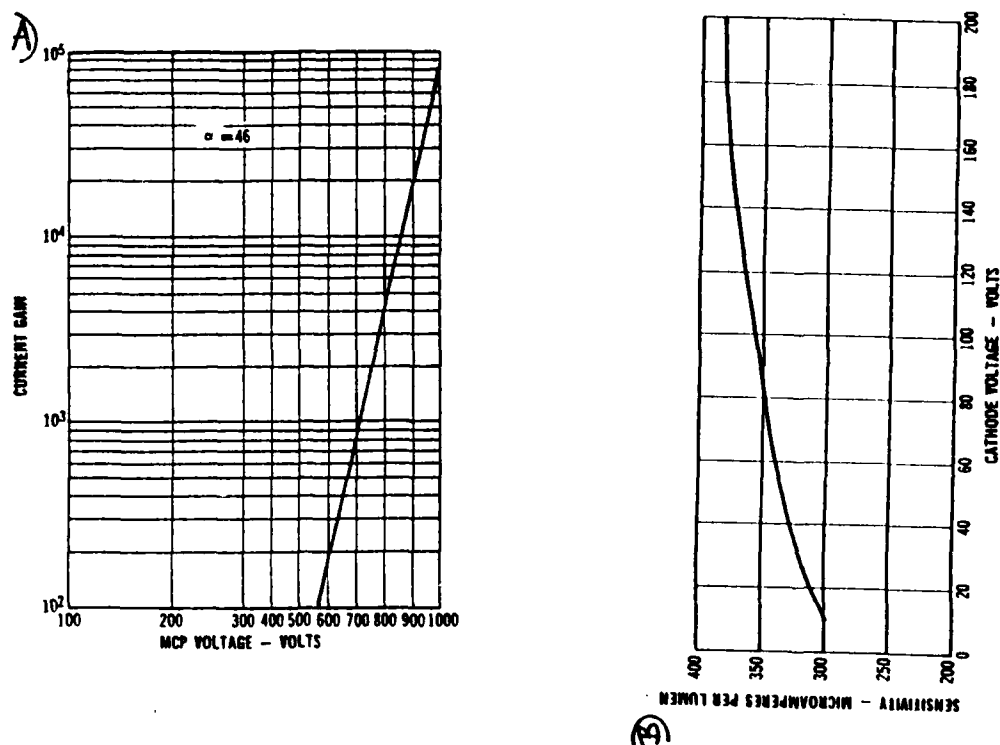


Figure 31. Relationships between Control Bias Voltages and Linear Component Gains for Typical Components of a Second Generation Image Tube. A) MCP current gain vs. MCP bias voltage [After Csorba (ref. 7)]; B) Luminous sensitivity vs. photocathode bias voltage [After Csorba]; C) Luminous output of a phosphor screen vs. phosphor screen accelerating potential [After Csorba].

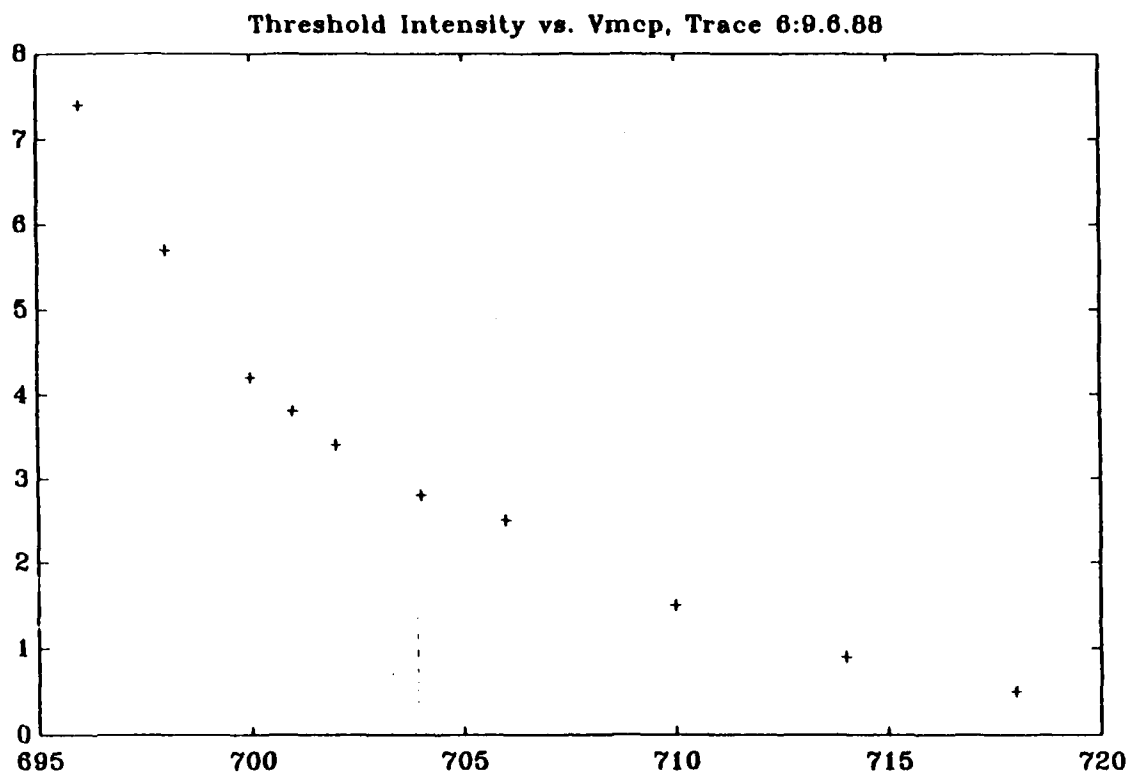


Figure 32. Input Threshold Intensity vs. MCP Bias Voltage, Measured.

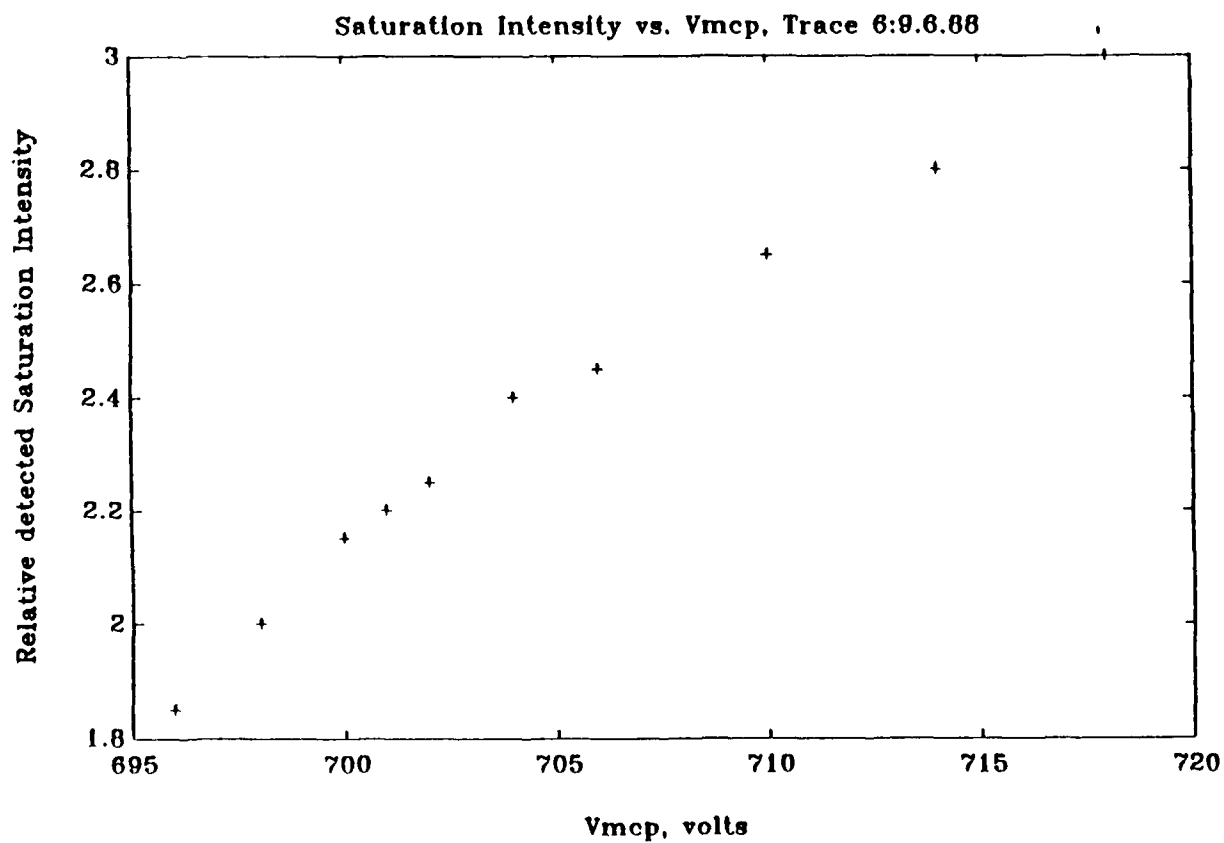


Figure 33. Output Saturation Intensity vs. MCP Bias Voltage, Measured.

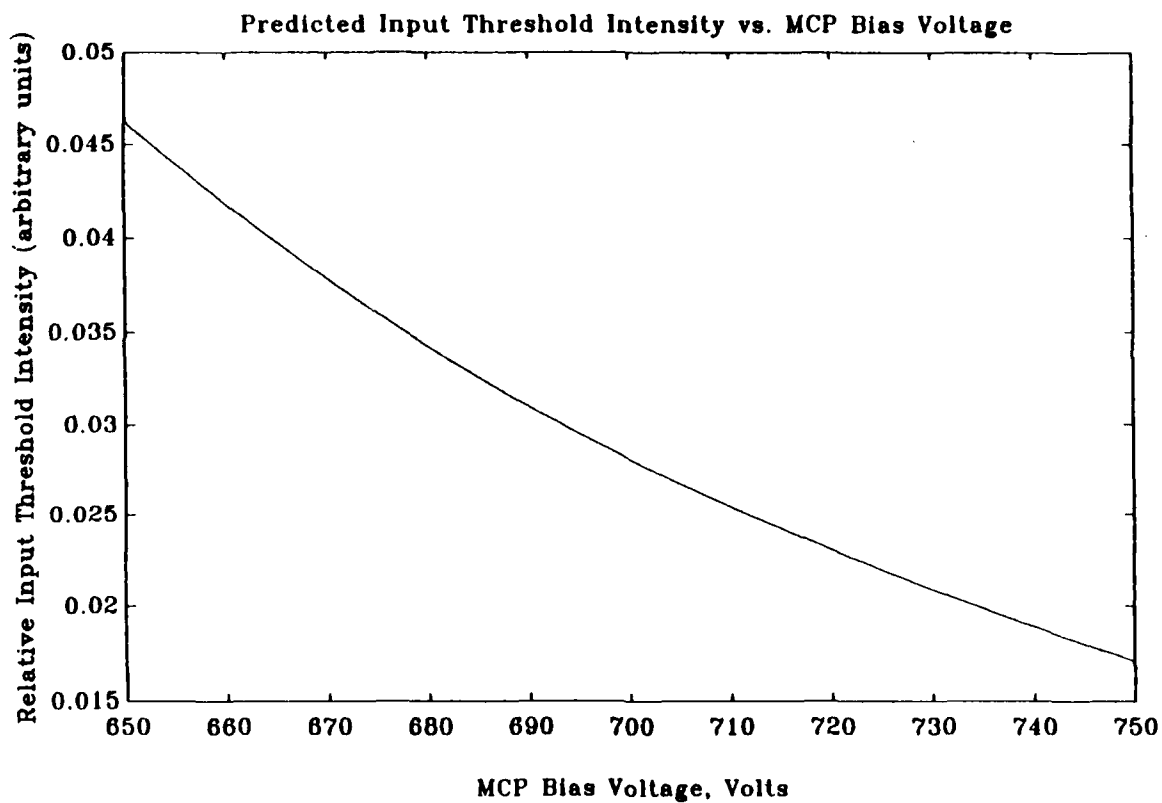


Figure 34. Input Threshold Intensity vs. MCP Bias Voltage Predicted by Monopixel IBOD Model.

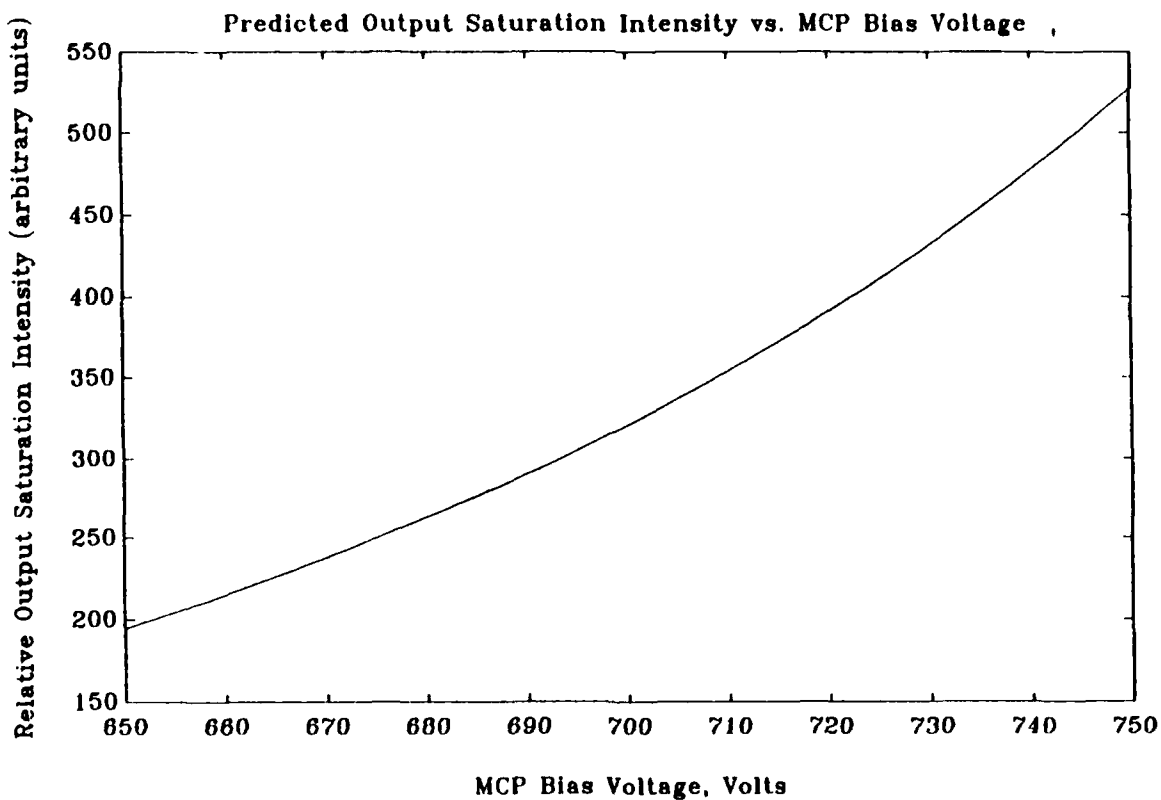


Figure 35. Output Saturation Intensity vs. MCP Bias Voltage Predicted by Monopixel IBOD Model.

compared with the measured results. The threshold intensity curve predicted thus compares reasonably well with the measured results: both predicted and measured curves show threshold decreasing with increasing MCP voltage, and both curves are convex. The measured data does vary more steeply with MCP voltage, but this may be due to variation of gain of the MCP from that predicted by Equation EQ-21. The saturation intensity curve predicted by the model does not compare as well. While the predicted curve correctly shows increasing saturation current with increasing MCP voltage, the predicted curve is convex, while the actual measured data follow a concave curve which flattens at higher voltages.

Figures 36 and 37 show the measured data for threshold and saturation intensities versus photocathode bias voltage. Compare these plots with the predicted curves of Figure 38 showing threshold and saturation intensities versus photocathode quantum efficiency. Assuming a linear relationship between quantum efficiency and bias voltage over the narrow range of interest, we find that the actual and measured threshold curves compare quite well, but the saturation curves again fail to match.

Figures 39 and 40 show both measured and predicted curves of threshold and saturation intensities versus phosphor screen accelerating potential. As before, the threshold prediction agrees with observation, the saturation prediction fails to agree.

Note that for all three control biases, the actual saturation dependence differed from the predicted dependence. This points to an inaccurate representation of the saturation phenomenon in the monapixel IBOD model. In particular, the actual model showed saturation intensity varying less with increasing component gains than predicted. This effect probably results from our choice of an overly simple model of the saturation effect in the IBOD. As mentioned in the model description, a more realistic representation would show the gain of the saturation component falling to zero with increasing input signal strength.

In contrast, the threshold intensity predictions agree reasonably well with the measured behavior. Thus the IBOD model adequately represents the thresholding behavior.

VI. RECOMMENDATIONS FOR FUTURE WORK

Three issues should be addressed by any program intended to make the IBOD a viable device: aging, temporal stability, and pixel blooming. We have collected sufficient information during the Phase I study to make some specific suggestions for approaching these issues.

The aging factor proved important in obtaining bistable behavior from the prototype devices, but its cause is not known. Observations made during the Phase I indicate that the phosphor is the likely source, but greater testing is required to confirm this. The fact that none of the prototypes were aged according to standard image tube manufacturing process may be related to the phenomenon. The aging process is of interest largely as a curiosity, however, since, once aged, the IBODs appear to function reliably. The long-term aging effects are unknown at this time and should be studied at length.

The lack of temporal stability in the IBOD prototypes is the most serious of the three issues, since it makes arbitrary placement of the switching threshold more

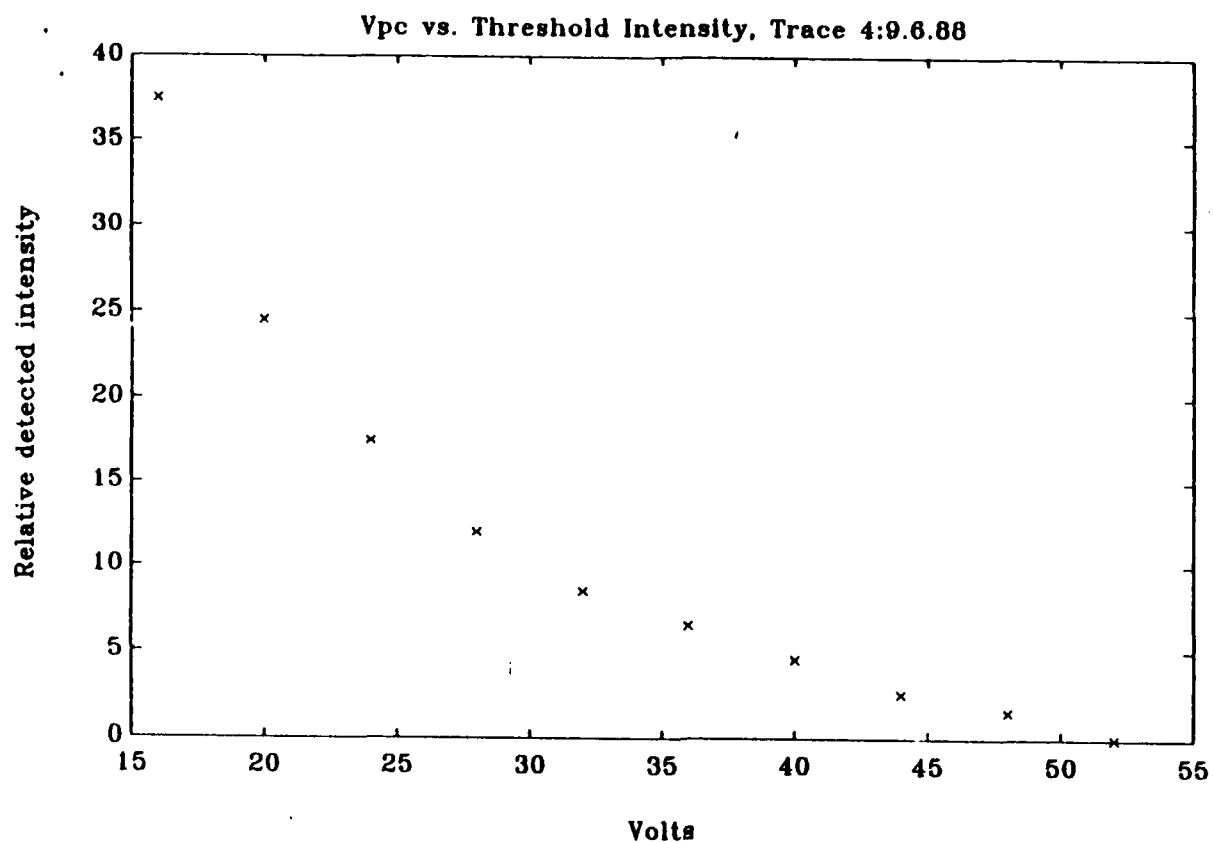


Figure 36. Input Threshold Intensity vs. Photocathode Bias Voltage, Measured.

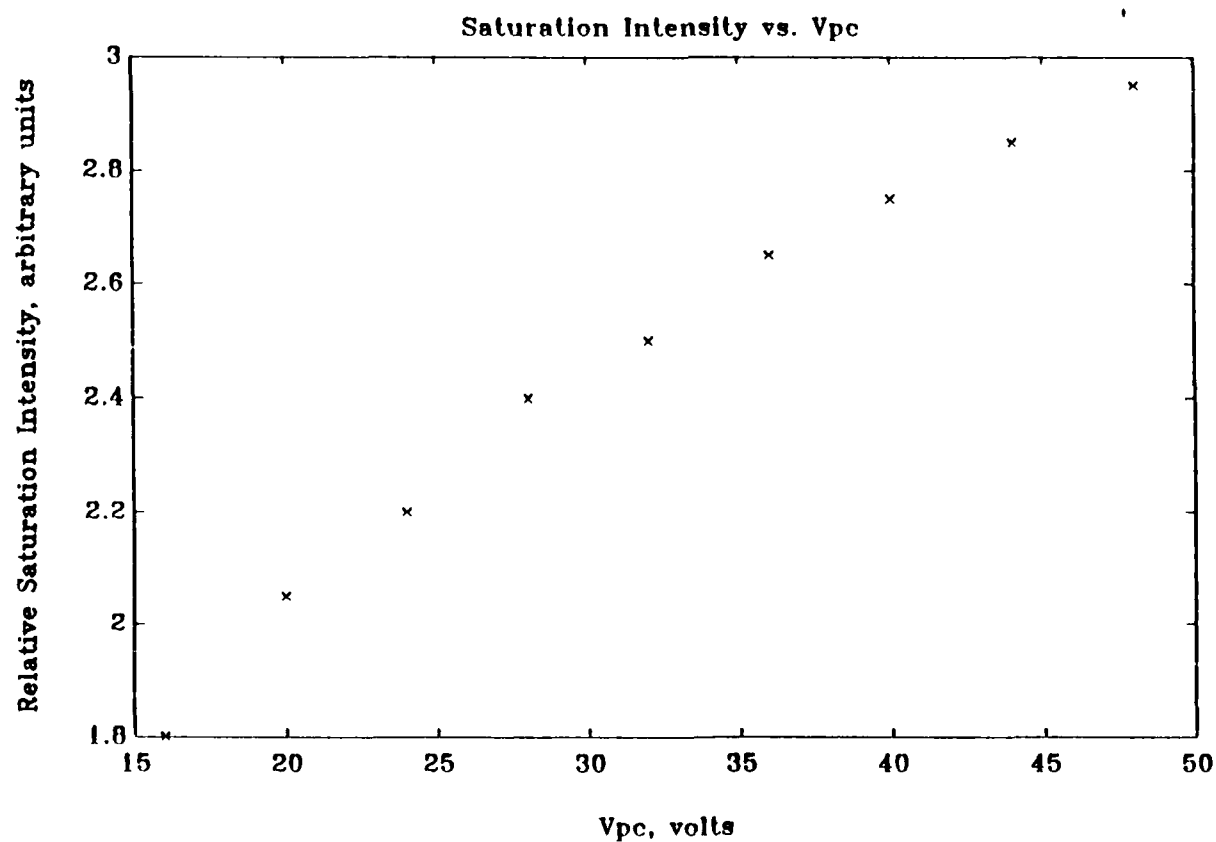


Figure 37. Output Saturation Intensity vs. Photocathode Bias Voltage, Measured.

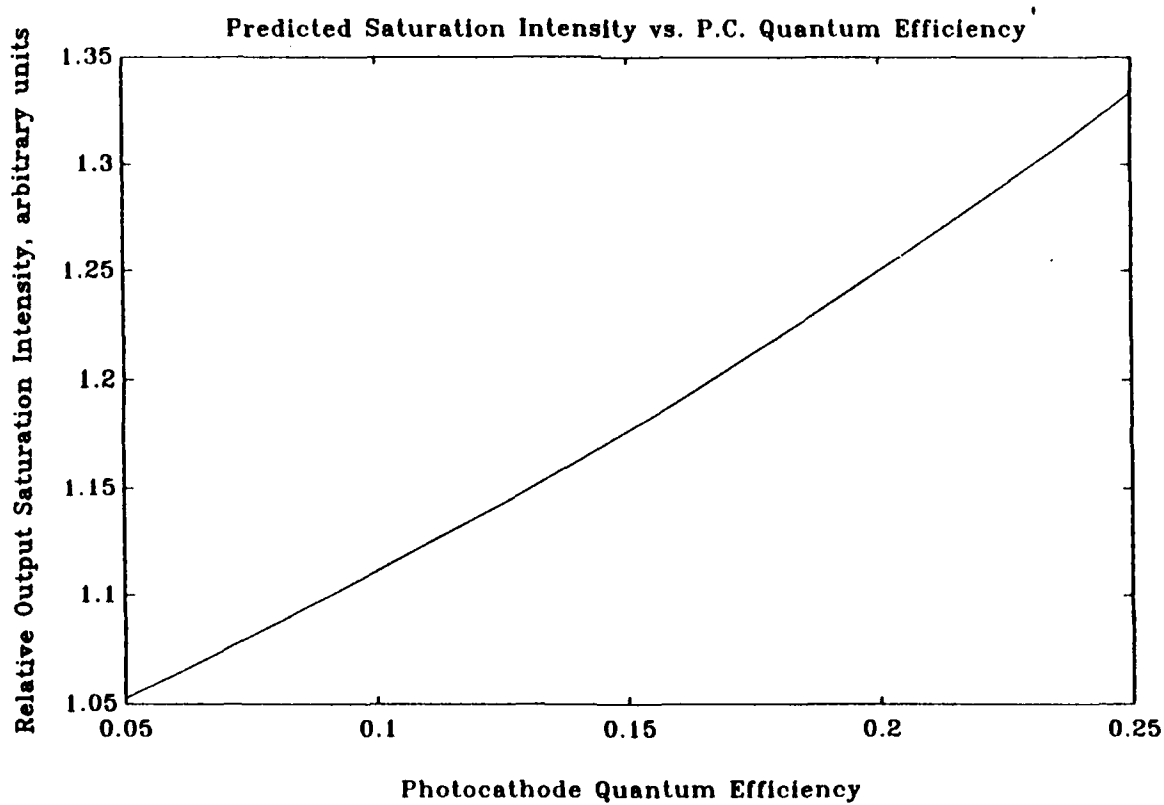
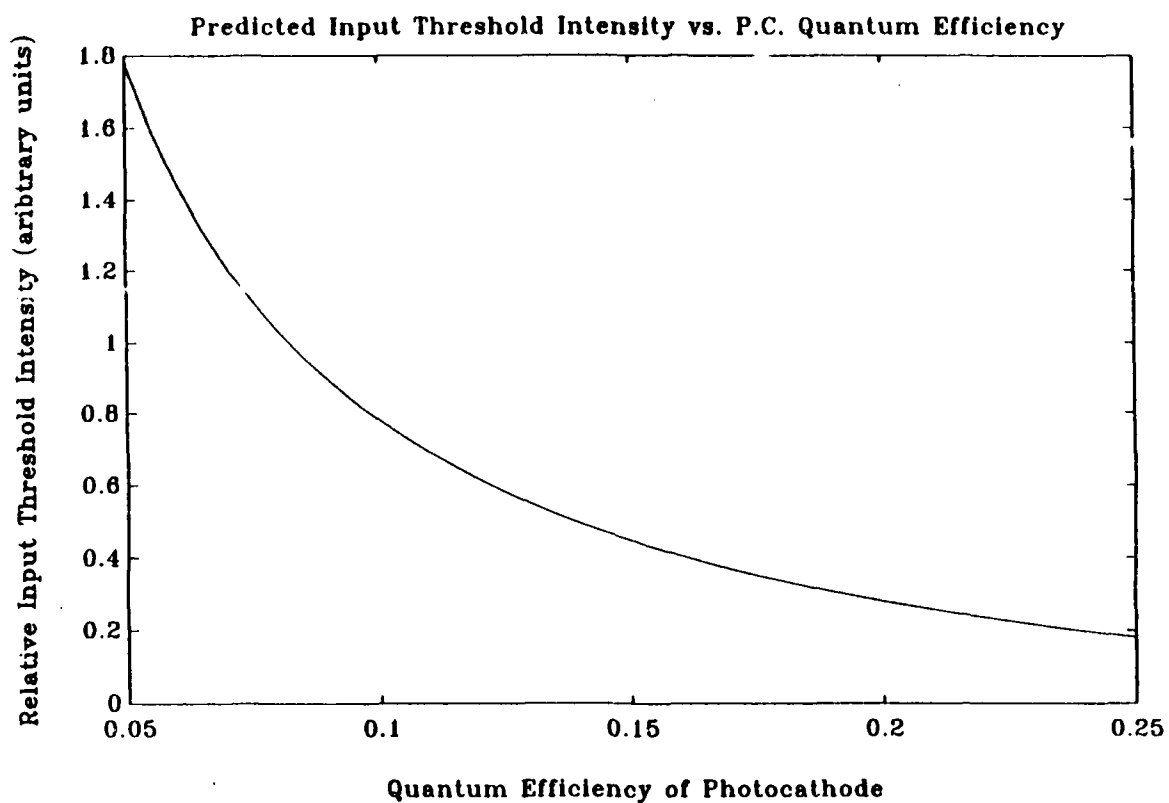


Figure 38. Predicted Curves for A) Input Threshold Intensity and B) Output Saturation Intensity vs. Photocathode Quantum Efficiency.

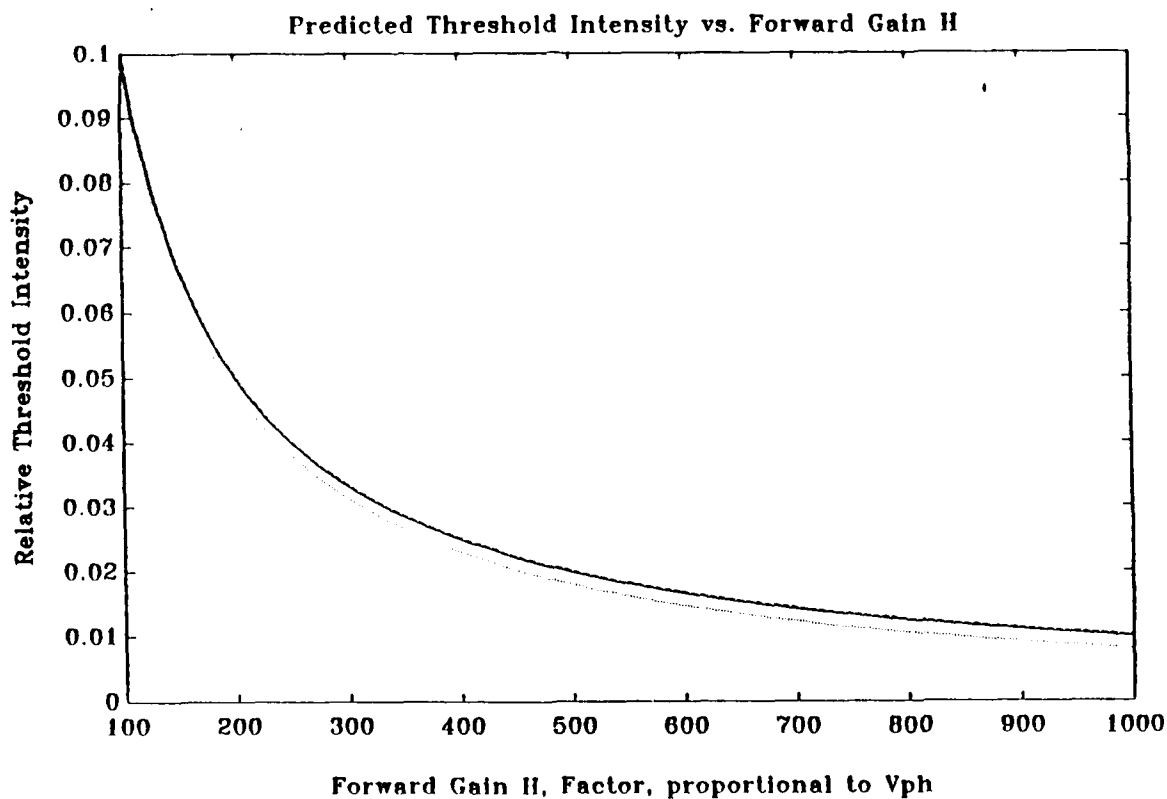
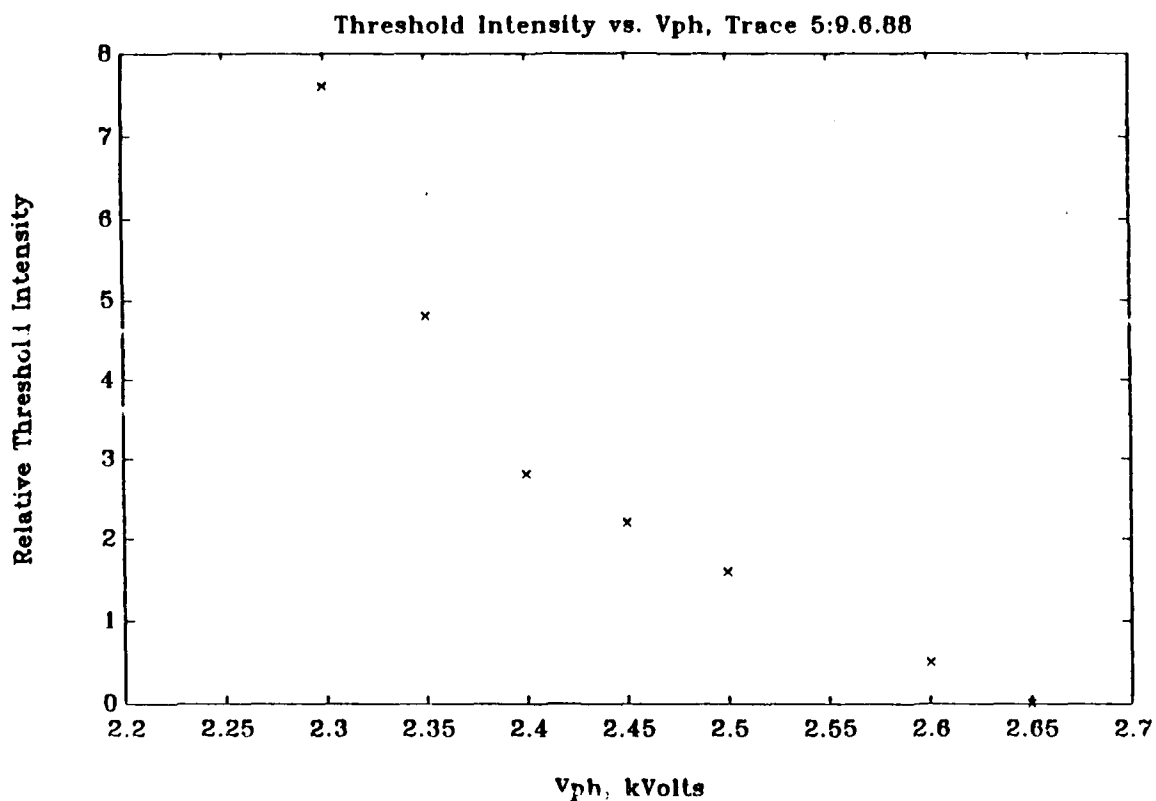


Figure 39. A) Measured and B) Predicted Curves for Input Threshold Intensity vs. Phosphor Screen Accelerating Potential V_{ph} . The predicted curves of B were generated from Equation EQ-10 assuming $u = i_d = 0$ and $\eta = 10\%$. For the solid line of B, $\eta JA = 2 \times 10^{-5}$ (best guess of actual case); for the dashed line, $\eta JA = 0$; for the dotted line $\eta JA = 2 \times 10^{-4}$.

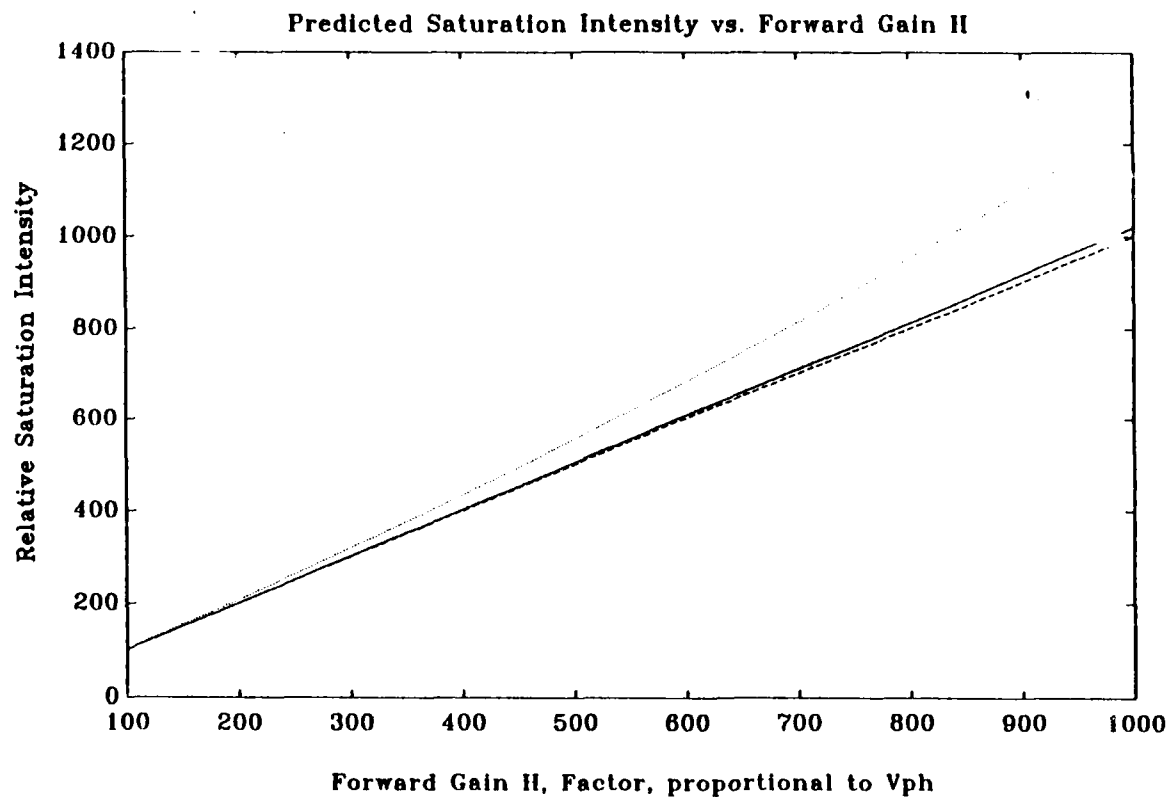
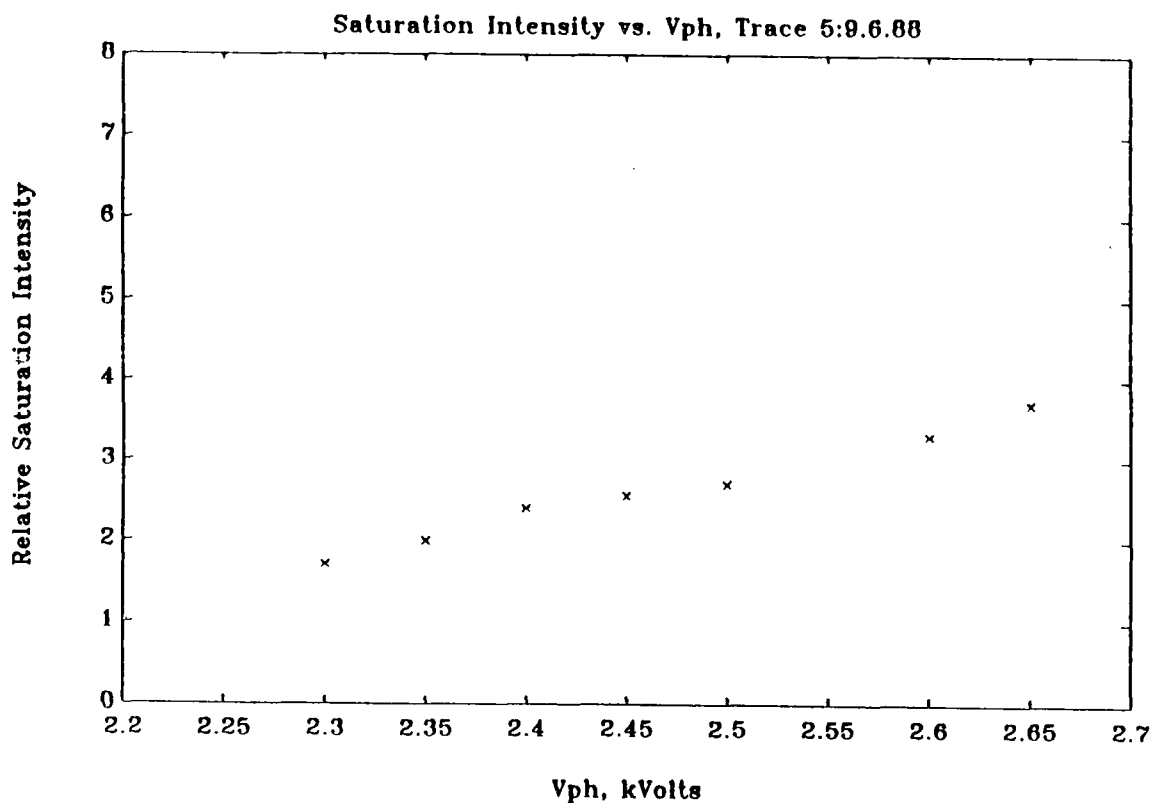


Figure 40. A) Measured and B) Predicted curves for Output Saturation Intensity vs. Phosphor Screen Accelerating Potential V_{ph} . The predicted curves of B were generated from Equation EQ-18 assuming $u = i_d = 0$. For the solid line of B, $\eta_{BJD} = 2 \times 10^{-5}$ (best guess of actual case); for the dashed line, $\eta_{BJD} = 0$; for the dotted line $\eta_{BJD} = 2 \times 10^{-4}$.

difficult. Observations made during Phase I have tentatively implicated the phosphor screen as the source. Since the phosphor is also suspected as the source of both the thresholding effect and the aging phenomenon, it is clear that any follow-on work should involve a careful study of the behavior of the phosphor screen. Once better understood, it may be possible to redesign the screen or employ another phosphor to minimize the effect of the temporal instability of the threshold. Nevertheless, even if the phenomenon turns out to be an inherent property of the phosphor, it should be possible to design a control circuit to compensate for the variation in threshold with time by varying one or more of the control biases.

The final issue which must be addressed by any IBOD development program is the crosstalk-induced pixel blooming problem. It appears that this may be more of a manufacturing problem than a technical problem, as we know the problem can be solved with the use of the proper pixel-confinement layers. Moreover, we suspect that the problem could most simply be solved by simplifying the architecture somewhat as in Figure 41. In this arrangement the photocathode abuts the MCP directly. A thin SiO_2 grid-like structure has been constructed directly on top of the MCP to allow the application of a small voltage bias between photocathode and MCP input. This bias can be used to gate the device quickly and easily. Between the output side of the MCP and the phosphor screen is a glass capillary array (GCA) to provide interpixel isolation. To guarantee minimal loss on the feedback path, the MCP is cut with a 0° bias angle so that the MCP channels and GCA channels are angle-aligned. This architecture should be somewhat simpler to build than one involving two pixel confinement layers and should provide near-perfect interpixel isolation.

Once these three issues have been addressed, the IBOD should easily be able to meet or exceed its predicted specifications.

VII. PHASE I CONCLUSIONS

Overall the Phase I program was quite successful, as the program demonstrated the bistability of the IBOD architecture. Externally programmable threshold and saturation intensities were demonstrated and measured as functions of the three device control biases. Moreover, a monapixel IBOD model was developed during the program which proved useful both in providing a better understanding of device function and in diagnosing prototype deficiencies. A functional prototype was constructed according to the final modified IBOD architecture which evolved during the Phase I program. Testing of the prototype confirmed the controllable bistability of the architecture and revealed three issues to be addressed by any potential follow-on programs. Some progress was made toward planning approaches for addressing these issues.

Unfortunately, another of the original Phase I goals, elimination of pixel-blooming, was not completely met. Though the process was studied and solutions were proposed, extensive delays in demonstrating bistability did not leave sufficient time for implementation of proposed pixel-blooming solutions. The delays were largely due to coordination problems with Varo, the company responsible for actual assembly of the prototypes. It became evident that the difficulty this manufacturing company had in implementing even the slightest innovations in their tube architecture would make construction of prototypes involving pixel-blooming solutions impossible. Thus we believe a successful follow-on effort should involve

direct construction of the prototypes by the group proposing the design innovations. In any Phase II effort, then, Optron Systems would construct prototypes on-site.

We believe that the potential for Phase II success is extremely high. We feel strongly that little additional innovation is absolutely necessary to solve the three issues which must be addressed to achieve a fully functional, manufacturable IBOD design, though the resulting solutions might be inelegant. With sufficiently innovative, properly funded follow-up program, however, simple and elegant solutions should be easily within reach. Such a program would begin with a period of research into the behavior of the phosphor in search of a thorough understanding of the aging and temporal stability problems, proceeding in parallel with construction of IBOD prototypes with pixel confinement mechanisms. Once the three issues had been satisfactorily resolved, a final prototype could be constructed incorporating all the final design modifications. With the knowledge acquired in the Phase I study, we are convinced that such a follow-on effort would be a low-risk investment with large potential returns in the advancement of optical computing technology.

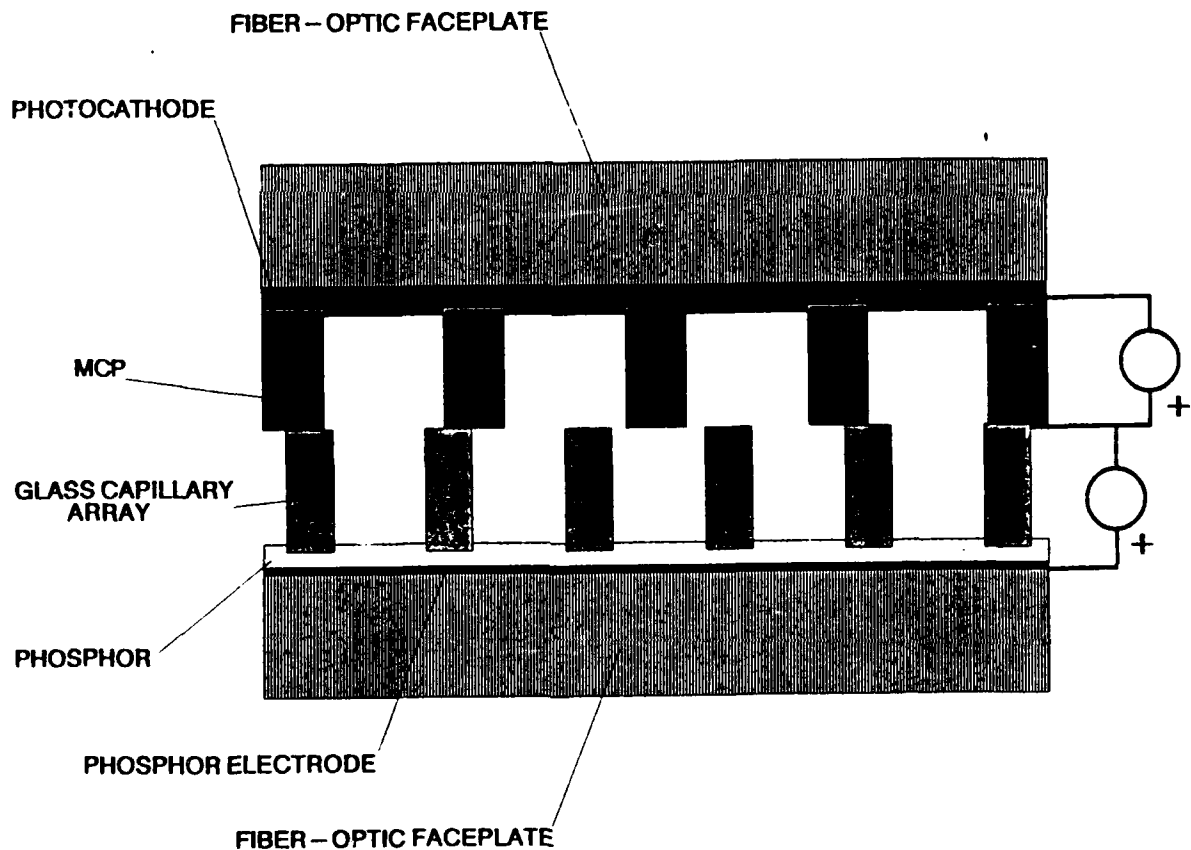


Figure 41. Proposed IBOD Architecture to Eliminate Crosstalk-Induced Pixel Blooming.

VIII. REFERENCES

1. H. M. Gibbs et al, "Room Temperature Excitonic Optical Bistability in a GaAs-GaAlAs super lattice Etalon," *Applied Phys. Lett.* **41**, 221 (1982)
2. J. L. Jewel et al, "Advances in GaAs Bistable Optical Devices," in *Optical Bistability 2*, C. M. Bowen, et al editors, Plenum, New York (1984)
3. S. D. Smith and F. A. P. Tooley, "Room Temperature Bistability, Logic Gate Operation Incoherent Switching and High Signal Gain with InSb Devices," in *Optical Bistability 2*, C. M. Bowen, et al, Editors, Plenum, New York, (1984)
4. A. K. Kar et al, *Appl. Phys. Lett.* **42**, 334 (1983)
5. S. D. Smith et al, "Room Temperature Wavelength Optical Bistability in ZnSe Interface Filters," *Optics Communications* **51**, 357-362 (1984)
6. W. F. Sharfin and M. Dagenais, "Room-Temperature Optical Bistability in InGaAsP/InP Amplifiers and Implications for Passive Devices," *Appl. Phys. Lett.* **46**, 819-821 (1985)
7. I. P. Csorba, *Image Tubes* (Howard W. Sams 1985, Indianapolis, Indiana) p. 240.

APPENDIX

In this Appendix we describe in some detail measurements of the optical transmission properties of the microchannel plate. Optical crosstalk occurs when optical feedback signals from adjacent pixels successfully propagate off-axis through the MCP, or when an on-axis signal diffracts upon leaving the MCP. Optical crosstalk at levels above threshold results in pixel blooming. The ideal MCP for the IBOD, then, exhibits a highly anisotropic transmissivity, attenuating strongly all optical signals except those travelling axially through its channels.

Experimental measurements on a straight-channel MCP using the apparatus of Figure A1 indicate a loss of only about 3 dB for a beam travelling axially along the channels of the MCP. The measurement involved passing a collimated He-Ne laser beam through the 3-cm-diameter MCP and measuring the resultant intensity just beyond the plate. Alignment of the MCP was achieved by adjusting the plate's orientation for maximum transmission. Results of measurements of transmitted intensity through the MCP for various angles of the incident beam are plotted in Figure A2.

A similar experimental apparatus was used to determine the radiation pattern of light emerging from the MCP (Figure A3). A He-Ne laser beam was focused onto a pinhole-covered, frosted glass plate diffuser to provide input light over a broad range of incident angles, simulating the effect of isotropically radiating phosphors. A pinhole covered photodetector was then used to measure intensity vs. output angle for the emerging light near the MCP. Results appear in Figure A4; note that detected output is quoted in decibels relative to the maximum (axial) output value, not to input intensity. Most of the spread of output is thought to be attributable to diffraction from the channels (rather than to transmission of non-axially propagating input light). Calculation of expected behavior from diffraction theory is difficult, however, since the phosphor layer of the prototype will lie between the near-field and far-field diffraction approximation regions.

APPARATUS FOR MEASUREMENT OF TRANSMISSION LOSS OF MCP

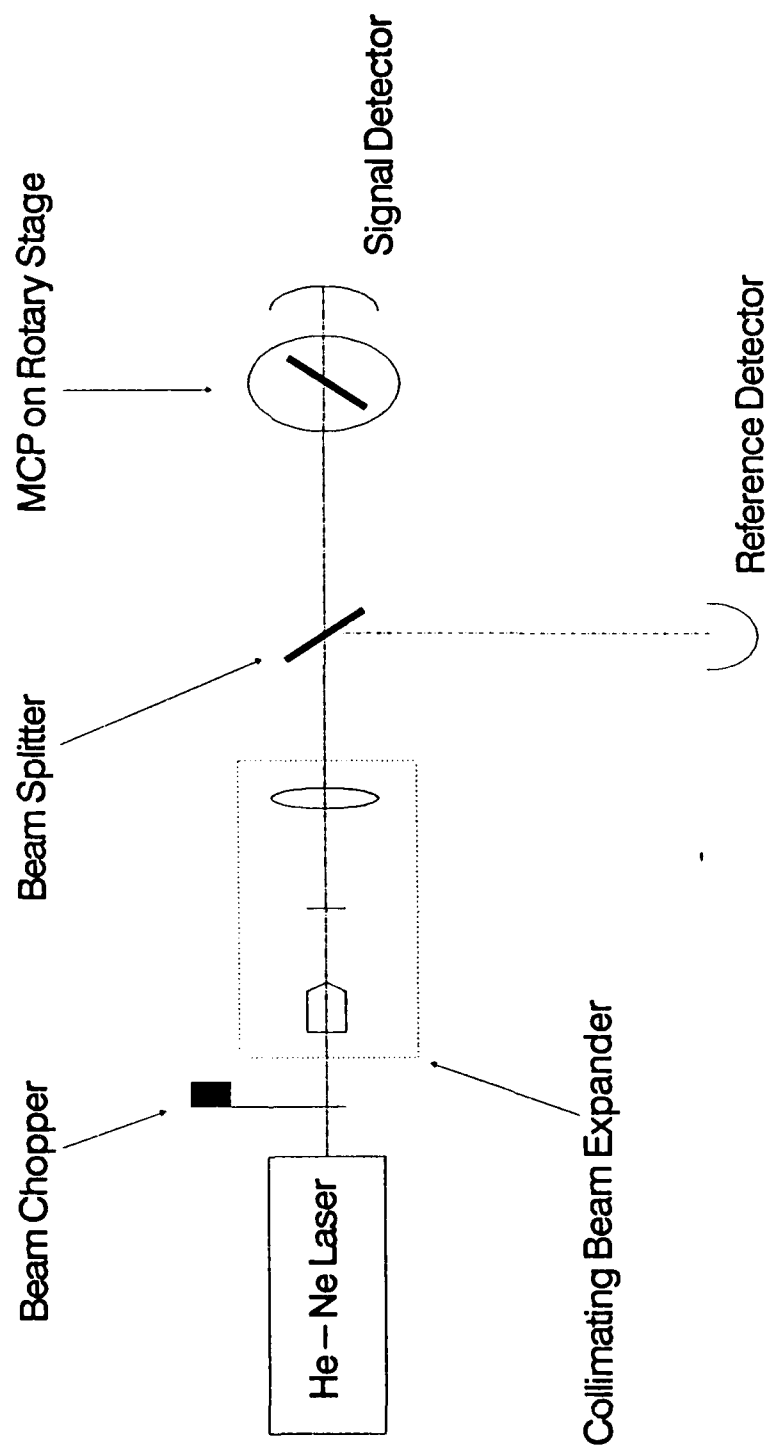


Figure A1. Apparatus Used to Measure Transmissivity of MCP for Light Entering MCP at Various Angles.

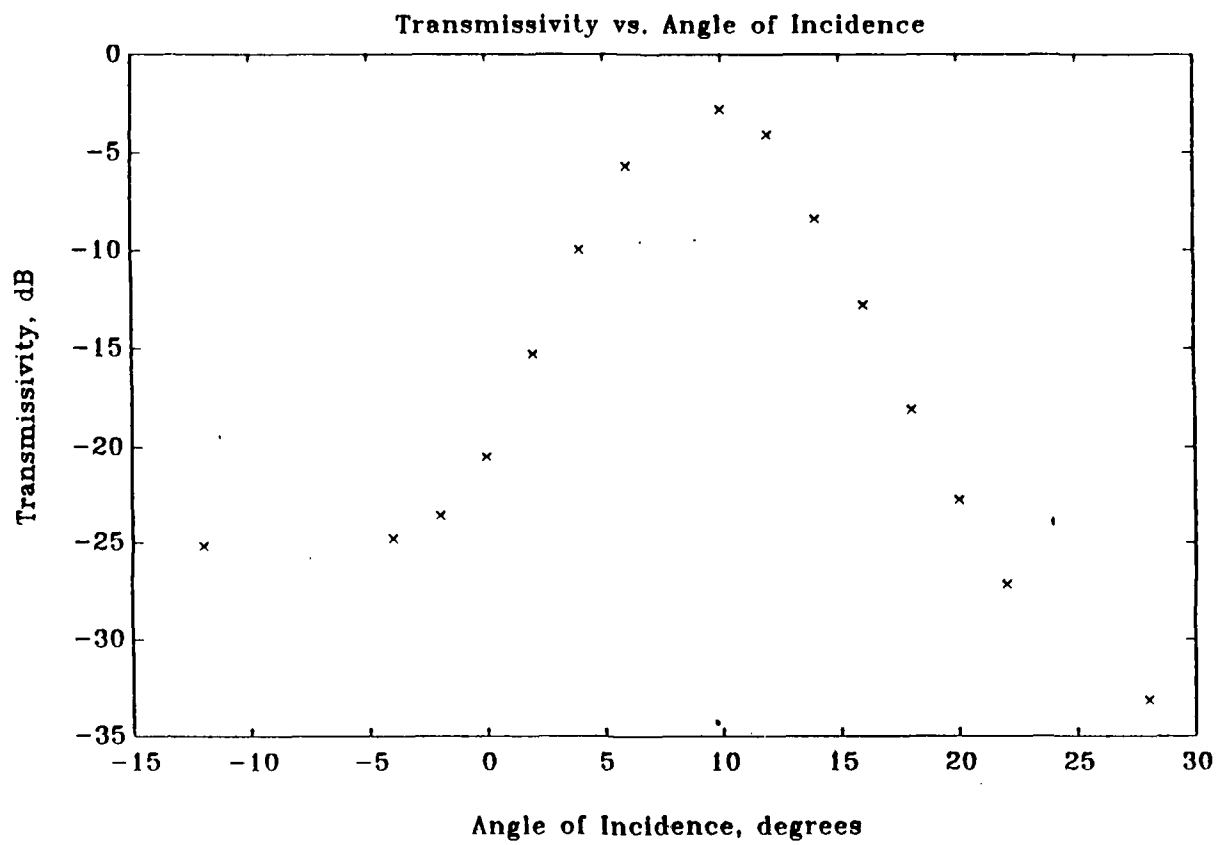


Figure A2. Optical Transmissivity of 10°-Bias Angle MCP vs. Angle of Incidence of Input Light.

APPARATUS FOR MEASUREMENT OF ANGULAR DISTRIBUTION OF TRANSMITTED LIGHT

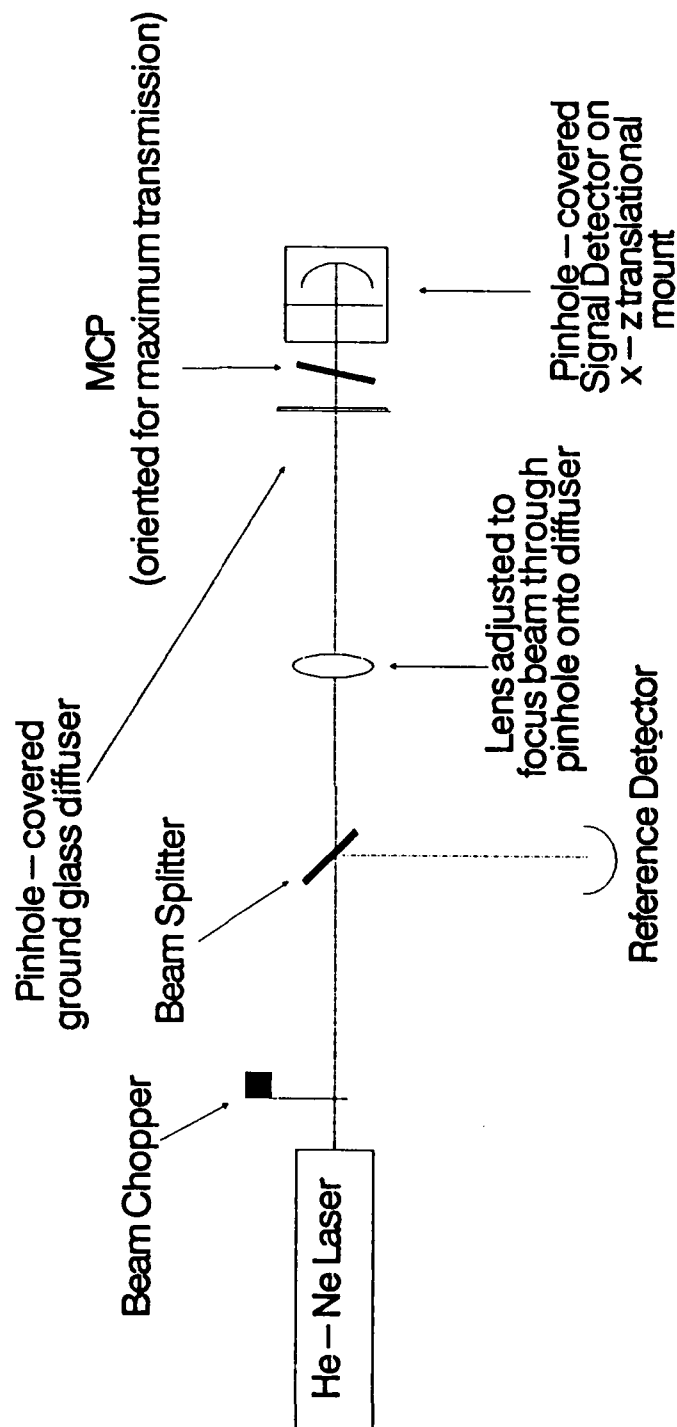


Figure A3. Apparatus Used to Measure Angular Distribution of Light Diffracted from by Transmission through MCP.

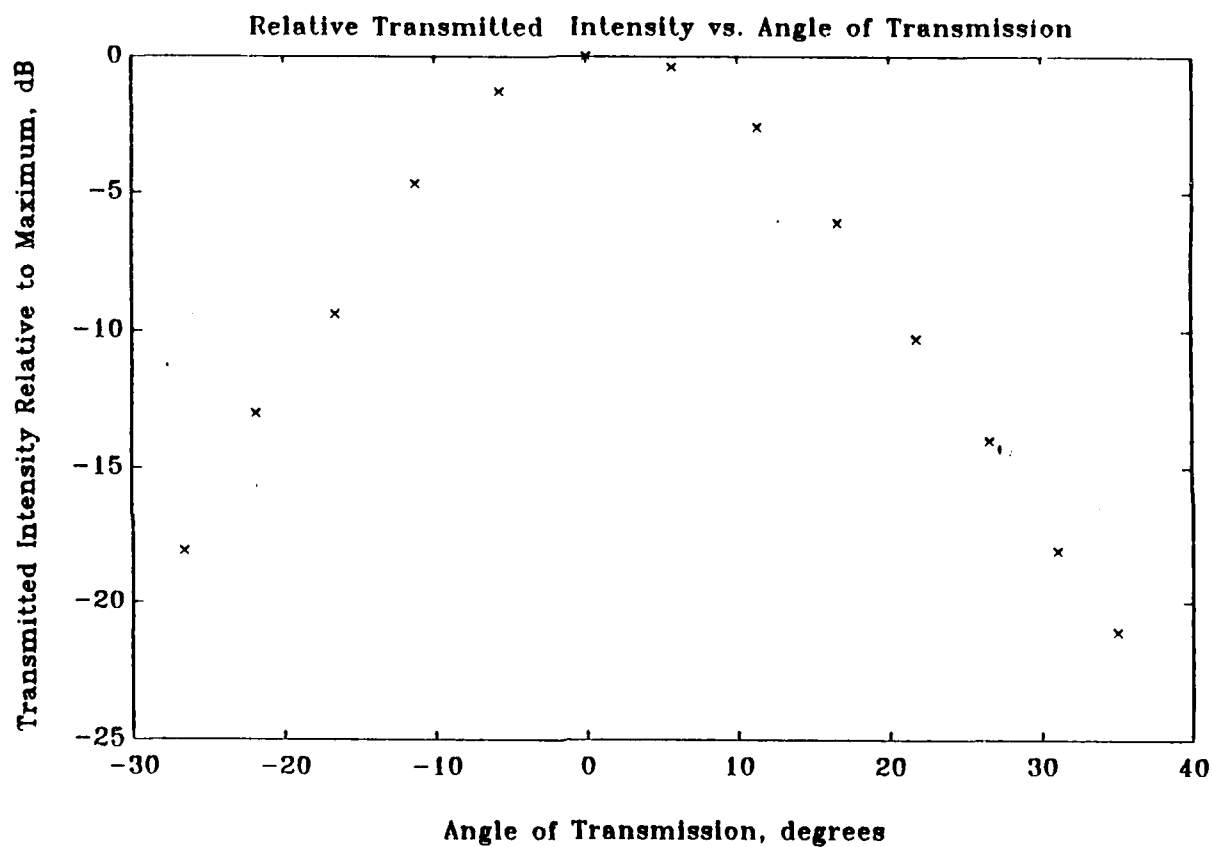


Figure A4. Angular Distribution of Light Diffracted by Transmission through MCP.
 Abscissa is transmission angle (Angle of Maximum Transmission $\equiv 0^\circ$);
 ordinate is relative intensity.